Belyaeva et al

1   **Cortical actin properties controlled by *Drosophila* Fos**

2   **aid macrophage infiltration against surrounding tissue resistance**

3   **Short title: Macrophage Cortical Actin counteracts Tissue Resistance**

4

5   **Vera Belyaeva[§1,2], Stephanie Wachner[§1], Igor Gridchyn[†1], Markus Linder[†3,4], Shamsi**

6   **Emtenani[1], Attila Gyoergy[1], Maria Sibilia[3], Daria Siekhaus[1*]**

7

8   §: These authors contributed equally

9   †: These authors contributed equally

10

11   *- Corresponding author, *daria.siekhaus@ist.ac.at*

12   *1 – Institute of Science and Technology Austria, Am Campus 1, 3400 Klosterneuburg,*

13   *Austria*

14   *2 – Current address: Molecular Devices, Urstein Süd 17, 5412, Austria*

15   *3 – Institute of Cancer Research, Department of Medicine 1, Comprehensive Cancer Center,*

16   *Medical University of Vienna, Austria*

17   *4 – Current address: F. Hoffmann‐La Roche Ltd.,Grenzacherstrasse 124, 4070 Basel,*

18   *Switzerland*

Belyaeva et al

19   **ABSTRACT**

20   The infiltration of immune cells into tissues underlies the establishment of tissue resident

21   macrophages, and responses to infections and tumors. Yet the mechanisms immune cells

22   utilize to negotiate tissue barriers in living organisms are not well understood, and a role for

23   cortical actin has not been examined. Here we find that the tissue invasion of *Drosophila*

24   macrophages, also known as plasmatocytes or hemocytes, utilizes enhanced cortical F-actin

25   levels stimulated by the *Drosophila* member of the fos proto oncogene transcription factor

26   family (Dfos, Kayak). RNA sequencing analysis and live imaging show that Dfos enhances

27   F-actin levels around the entire macrophage surface by increasing mRNA levels of the

28   membrane spanning molecular scaffold tetraspanin TM4SF, and the actin cross-linking

29   filamin Cheerio which are themselves required for invasion. Cortical F-actin levels are

30   critical as expressing a dominant active form of Diaphanous, a actin polymerizing Formin,

31   can rescue the *Dfos* Dominant Negative macrophage invasion defect. *In vivo* imaging shows

32   that Dfos is required to enhance the efficiency of the initial phases of macrophage tissue

33   entry. Genetic evidence argues that this Dfos-induced program in macrophages counteracts

34   the constraint produced by the tension of surrounding tissues and buffers the mechanical

35   properties of the macrophage nucleus from affecting tissue entry. We thus identify tuning

36   the cortical actin cytoskeleton through Dfos as a key process allowing efficient forward

37   movement of an immune cell into surrounding tissues.

38

39   **Introduction**

40   The classical model of cell migration on a surface postulated in the 1980's by

41   Abercrombie has been extended (Danuser et al., 2013) by studies showing that migrating

42   cells utilize diverse strategies depending on the architecture and physical properties of their

43   three dimensional (3D) surroundings (Paluch et al., 2016). Much of this work has been

44 conducted *in vitro*, where variations in the environment can be strictly controlled. However

45 most 3D migration occurs within the body, and much less research has elucidated the

46 mechanisms used to efficiently move in these diverse environments, particularly into and

47 through tissues. Such migration is crucial for the influence of the immune system on health

48 and disease. Vertebrate macrophages migrate into tissues during development where they

49 take up residence, regulating organ formation and homeostasis and organizing tissue repair

50 upon injury (Ginhoux and Guilliams, 2016; Theret et al 2019). A variety of types of immune

51 cells infiltrate into tumors, and can both promote or impede cancer progression (Greten and

52 Grivennikov 2019; Sharma and Allison, 2015). Responses to infection require immune cells

53 to traverse through the vascular wall, into the lymph node, and through tissues (Luster et al.,

54 2005). Yet the mechanisms utilized by immune cells to allow migration into such

55 challenging cellular environments *in vivo* are not well understood.

56   Migration in 2-D and 3-D environments utilizes actin polymerization to power

57 forward progress. The assembly of actin at the leading edge, when coupled to Integrin

58 adhesion to anchor points in the surrounding ECM, can allow the front of the cell to progress

59 (Mitchison and Cramer, 1996). This anchoring also allows the contraction of cortical actin

60 at the rear plasma membrane to bring the body of the cell forwards. But a role for

61 crosslinked actin at the cell surface in assisting forward progress by helping to counteract the

62 resistance of surrounding tissues and in buffering nuclear properties has not been previously

63 identified.

64   Our lab utilizes *Drosophila* macrophage migration into the embryonic germband (gb)

65 to investigate mechanisms of immune cell tissue invasion. Macrophages, also called

66 plasmatocytes or hemocytes, are the primary phagocytic cell in *Drosophila* and share

67 striking similarities with vertebrate macrophages (Brückner et al., 2004; Evans & Wood,

68 2011; Lemaitre & Hoffmann, 2007; Ratheesh et al., 2015; Weavers et al., 2016). They are

69   specified in the head mesoderm at embryonic stages 4-6 and by stage 10 start spreading

70   along predetermined routes guided by platelet-derived growth factor- and vascular

71   endothelial growth factor-related factors (Pvf) 2 and 3 (Cho et al., 2002; Brückner et al.,

72   2004; Wood et al., 2006) to populate the whole embryo. One of these paths, the movement

73   into the gb, requires macrophages to invade confined between the ectoderm and mesoderm

74   (Ratheesh et al., 2018; Siekhaus et al., 2010). The level of tension and thus apparent

75   stiffness of the flanking ectoderm is a key parameter defining the efficiency of macrophage

76   passage into and within the gb (Ratheesh et al., 2018). Penetration of macrophages into the

77   gb utilizes Integrin, occurs normally without MMPs (Siekhaus et al., 2010) and is even

78   enhanced by ECM deposition (Valoskova et al., 2019; Sánchez-Sánchez et al., 2017) likely

79   because the basement membrane has not yet formed at this stage (Matsubayashi et al., 2017;

80   Ratheesh et al., 2018). Thus *Drosophila* macrophage gb invasion represents an ideal system

81   to explore the mechanisms by which immune cells and surrounding tissues interact with one

82   another to aid the invasion process.

83   Here we sought to identify a transcription factor that could control immune cell tissue

84   invasion and elucidate its downstream mechanisms. We identify a role for the *Drosophila*

85   ortholog of the proto-oncogene Fos, in initial entry and migration within the tissue. We find

86   Dfos increases cortical macrophage F-actin levels through the formin Cheerio and the novel

87   target the tetraspanin TM4SF, aiding macrophages to move forward against the resistance of

88   the surrounding tissues while buffering the mechanical properties of the nucleus.

89   **Results**

90   **The transcription factor Dfos is required for macrophage germband invasion**

91   To identify regulators of programs for invasion we searched the literature for

92   transcription factors in macrophages prior to or during their invasion of germband tissues

93   (gb) (Fig 1A-B'). Of the 12 such factors (S1 Table, based on Hammonds et al., 2013) we

94   focused on Dfos, a member of the Fos proto-oncogene family, assigned by the Roundup

95   algorithm as being closest to vertebrate c-fos (Deluca et al., 2012; Thurmond et al., 2019)

96   (Fig 1C). Dfos contains the basic leucine zipper domain (bZIP) shown to mediate DNA

97   binding and hetero and homo dimerization (Glover and Harrison, 1995; Szalóki et al., 2015)

98   with the third leucine replaced by a methionine, a position also altered in the *C. elegans*

99   ortholog FOS-1A (Sherwood et al., 2005). Embryo *in situ* hybridizations reveal enriched

100   expression of the gene in macrophages at early stage 11 (Fig 1D, arrow) which is attenuated

101   by stage 13. Dfos protein appears in the nucleus in a subset of the macrophages that are

102   migrating towards the gb at stage 10-11 and in all macrophages by early stage 12 (Fig 1E-F'

103   yellow arrowheads, G-G''' white arrows) persisting through stage 13 (S1A Fig). The $Dfos^1$

104   null mutant eliminates the macrophage signal, indicating antibody specificity (Fig 1H). To

105   determine if Dfos affects invasion, we examined the 70% of embryos from $Dfos^1$ and the

106   hypomorph $Dfos^2$ that did not display developmental defects at these early stages; we

107   quantified macrophage numbers in the gb during a defined development period in early

108   stage 12 (Fig 1M). Both Dfos mutants displayed significantly reduced numbers of

109   macrophages in the gb compared to the control (Fig 1I-K, N) with normal numbers in the

110   pre-gb zone for $Dfos^2$ (S1B Fig) (S1 Data). Macrophage-specific expression of *Dfos* rescues

111   the $Dfos^2$ mutant (Fig 1L,N). Blocking Dfos function in macrophages with a dominant

112   negative (DN) Dfos (Fig 1O-Q) that lacks the activation domain but retains the capacity to

113   dimerize and bind DNA (Eresh et al., 1997) or two different RNAis against *Dfos* (Fig 1R)

114   recapitulates the decrease in gb macrophages seen in the null while not affecting

115   macrophage numbers in the whole embryo (S1C Fig), neighboring the germband (S1D Fig)

116   and along the ventral nerve cord (vnc); (S1E-F Fig). These results argue that Dfos is

117   required in macrophages for their migration into the gb. Since overexpressing DfosDN in

118   the midgut does not inhibit a bZIP protein that acts there (Eresh et al., 1997) and

Belyaeva et al

119   overexpressing Dfos in macrophages does not change gb numbers (S1G Fig), Dfos and

120   DfosDN do not appear to inhibit other bZIP proteins at higher levels of expression. As

121   DfosDN should exert a quicker effect than RNAis, further experiments examining Dfos' role

122   in enhancing germband invasion utilized mostly the DN form.

123   **Fig 1. The bZIP transcription factor Dfos acts in macrophages to facilitate their**

124   **migration into the germband**

125   Schematics of lateral **(A)** stage (St) 11 and **(A')** early St 12 embryos. The boxed region

126   magnified below indicates where macrophages (green) invade the germband (gb) after

127   moving there from the head **(B-B')**. Macrophages sit on the yolk sac (yellow) next to the

128   amnioserosa (black llne) and then invade between the ectoderm (blue) and mesoderm

129   (purple).

130   **(C)** Dfos protein aligned with its human orthologs c-Fos and FosB; orange outlines the

131   bZIP region that has 48% identity to both proteins: identical amino acids shown in orange,

132   conserved ones in green. Stars indicate Leucines in the zipper; ^ the third leucine which in

133   Dfos is a methionine, a tolerated substitution (Garcia-Echeverria, 1997). The lower solid

134   line indicates the basic domain and the dotted line the leucine zipper (ZIP).

135   **(D)** *In situ* hybridization of St 11 and 13 embryos with a riboprobe for Dfos-RB

136   (Fbcl0282531) which also detects all Dfos isoforms. *Dfos* RNA expression is enriched in

137   macrophages (arrow) and the amnioserosa (arrowhead) before gb invasion, but is gone

138   thereafter.

139   **(E-H')** Confocal images of the boxed region in A from fixed embryos expressing *GFP* in

140   macrophages (green) stained with a Dfos Ab (red). **(E-F', H-H')** A white dashed line

141   indicates the gb edge. **(E-F)** The Dfos Ab (yellow arrowheads) stains **(E)** a subset of the

142   macrophages moving towards the gb at St 11, and **(F)** all macrophages by early St 12, as

143   well as the amnioserosa (white arrowheads). **(G)** Higher magnification shows Dfos

144   colocalizing with the nuclear marker DAPI (white). **(H)** No staining is detected in

145   macrophages or the amnioserosa in the null *Dfos¹* mutant.

146   **(I-L)** Lateral views of mid St 12 embryos from **(I)** the control, **(J)** the null allele *Dfos¹*, **(K)**

147   the hypomorphic allele *Dfos²*, and **(L)** *Dfos²* with *Dfos* re-expressed in macrophages.

148   **(M)** Schematic of St 12 embryo, gb region indicated by a black oval outline. **(N)**

149   Quantitation reveals that both *Dfos* alleles display fewer macrophages in the gb. Re-

150   expression of *Dfos* in macrophages in the *Dfos²* hypomorph significantly rescues the defect.

151   Control vs. *Dfos¹* p=0.02 (30% reduction), Control vs. *Dfos²* p=0.017 (25% reduction),

152   Control vs. *Dfos²; mac>Dfos* p=0.334.

153   **(O-P)** Lateral views of mid St 12 embryos from **(O)** the control, or **(P)** a line expressing a

154   dominant negative (DN) form of Dfos in macrophages. **(Q)** Quantification of macrophage

155   numbers in the gb (see schematic) in the two genotypes visualized in **O**, **P**. p<0.0001(****)

156   (41% reduction).

157   **(R)** Quantification of macrophage numbers in the gb of the control and two different lines

158   expressing RNAi constructs against Dfos in macrophages. Control vs. *Dfos RNAi¹* (TRiP

159   HMS00254) p=0.001 (32% reduction), Control vs. *Dfos RNAi²* (TRiP JF02804) p=0.02 (21%

160   reduction). The data in **Q** and **R** argue that Dfos is required within macrophages to promote

161   gb tissue invasion.

162   Embryos are positioned with anterior to left and dorsal up in all images and histograms show

163   mean + standard error of the mean (SEM) throughout. Macrophages are labeled using *srp-*

164   *Gal4* ("mac>") driving *UAS-GFP* in **E-H**, *UAS-GFP::nls* in **I-L** and *srpHemo-*

165   *H2A::3xmCherry* in **O-P**. ***p<0.005, **p<0.01, *p<0.05. One-way ANOVA with Tukey

166   post hoc was used for **N** and **R**, and unpaired t-test for **Q**. The embryo number analysed is

167   indicated within the relevant column in the graphs. Scale bar: 50 μm in **D**, 5 μm in **E-H** and

168   10 μm in **I-L, O-P**.

169   **Dfos promotes macrophage motility and persistence during tissue entry**

170   To examine the dynamic effects of Dfos on tissue invasion, we performed live imaging and

171   tracking of macrophages. We visualized macrophages with *srpHemo-H2A::3xmCherry*

172   (Gyoergy et al., 2018) in either a wild type or *mac>DfosDN* background, capturing the

173   initial stage of invasion (S1 Movie). The speed of macrophages moving in the area

174   neighboring the germband prior to invasion was not significantly changed (pre-gb, Fig

175   2B,C). However, the first *mac>DfosDN* macrophage to enter is delayed by 20 min in

176   crossing into the gb (Fig 2D). *mac>DfosDN* macrophages also displayed reduced speed and

177   directional persistence during entering as well as while moving along the first 20μm of the

178   ectoderm-mesoderm interface (gb entry, Fig 2E, S2A Fig). Macrophages in the *Dfos²* mutant

179   largely mirrored this phenotype, but displayed slower movement in the pre-gb zone

180   neighboring the amnioserosa in which Dfos is also expressed (Fig 1D-F), likely causing a

181   non-autonomous effect (S2B-C Fig, S2 Movie) (Fig 1D, black arrowhead, E-F, white

182   arrowheads). Macrophages expressing DfosDN moved with unaltered average speed as they

183   spread out along the non-invasive route of the vnc (Fig 2F, Fig 2G, S3 Movie), albeit with

184   reduced directional persistence (S2A Fig). We thus conclude from live imaging that Dfos in

185   macrophages aids their initial invasive migration into the gb, increases their speed within the

186   gb and does not underlie their progress along the vnc.

187   **Fig 2. Dfos facilitates the initial invasion of macrophages into the gb tissue**

188   (**A**) Movie stills of control embryos and those expressing DfosDN in macrophages (green,

189   labelled using *srpHemo-H2A::3xmCherry*). Area imaged corresponds to the black dashed

190   square in the schematic above. The germband (gb) border is outlined with a white dashed

191   line. The first entering macrophage is indicated with a white arrowhead, and time in minutes

192   in the upper right corner.

193   (**B**) Detailed schematic showing the different zones for which the parameters of macrophage

194   gb invasion were quantified. The pre-gb area is shown in yellow, the gb entry zone is outlined

195   in a solid line.

196   (**C**) Macrophage speed in the pre-gb area was not significantly changed in macrophages

197   expressing DfosDN (3.00 μm/min) compared to the control (3.61 μm/min), p= 0.58.

198   (**D**) Quantification shows a 68% increase in the total gb crossing time of DfosDN expressing

199   macrophages compared to the control. Total gb crossing time runs from when macrophages

200   have migrated onto the outer edge of the gb ectoderm, aligning in a half arch, until the first

201   macrophage has translocated its nucleus into the gb ecto-meso interface. p=0.008.

202   (**E**) DfosDN expressing macrophages displayed a significantly reduced speed (1.53 μm/min)

203   at the gb entry zone compared to the control (1.98 μm/min), p= $1.11e^{-06}$.

204   (**F**) Macrophages expressing DfosDN in a Stage 13 embryo move with unaltered speed along

205   the vnc in the region outlined by the dashed black box in the schematic above (4.93

206   μm/min), compared to the control (4.55 μm/min), p= 0.64. Corresponding stills shown in (**G**)

207   Macrophages are labeled by *srpHemo-Gal4* driving *UAS-GFP::nls*.

208   ***p<0.005, **p<0.01, *p<0.05. Unpaired t-test used for **C-F**, a Kolmogorov-Smirnov test

209   for **D.** For each genotype, the number of tracks analysed in **C** and **F,** and the number of

210   macrophages in **D-E** are indicated within the graph columns. Tracks were obtained from

211   movies of 7 control and 7 *mac>DfosDN* expressing embryos in panel **D**, 3 each in **C, F**, and

212   4 each in **E**. Scale bar: 10 μm.

Dfos modulates Filamin and Tetraspanin to aid gb tissue invasion

213   To identify Dfos targets that promote macrophage invasion, we FACS isolated

214   macrophages from wild type and *mac>DfosDN* embryos during the time when invasion has

215   just begun, and conducted RNA-sequencing of the corresponding transcriptomes (Fig 3A, S1

216   Data). We first assessed reads that map to Dfos, which can correspond to both endogenous

217   and DfosDN mRNA; we found a 1.6 fold increase in the presence of the one copy of DfosDN

218   in this line, arguing that this transgene is expressed at levels similar to each endogenous copy

219   of Dfos and is unlikely to produce extraneous effects (S2 Data). We then examined genes that

220   in the presence of DfosDN displayed a log2 fold change of at least 1.5 with an adjusted P

221   value less than 0.05.10 genes were down-regulated (Fig 3B, S3A-B Fig) and 9 up-regulated

222   by DfosDN (S2 Table). Upregulated genes in DfosDN encoded mostly stress response

223   proteins, so we concentrated on the downregulated class. Of these, we focused on the actin

224   crosslinking filamin Cheerio (Cher) and the tetraspanin TM4SF from a group that can form

225   membrane microdomains that affect signalling and migration (Razinia et al., 2012; Yeung et

226   al., 2018). No known role for TM4SF had been previously identified in *Drosophila*. To

227   determine if these Dfos targets were themselves required for invasion, we RNAi knocked

228   down Cher and TM4SF through RNAi individually or simultaneously and observed

229   significantly reduced macrophage numbers in the gb, particularly upon the knockdown of

230   both targets simultaneously (Fig 3C-G) while not affecting macrophage numbers in the pre-

231   gb zone (S3D Fig) or on the vnc (S3E Fig). Over-expression of Cher or TM4SF along with

232   *DfosDN* in macrophages increased the mean macrophage numbers in the gb, and over-

233   expression of TM4SF rescued the *DfosDN* macrophage invasion defect (Fig 3H-L).

234   Expression of a GFP control did not restore macrophage invasion indicating that the rescue

235   we observed through Cher or TM4SF expression was not due to promoter competition

236   leading to reductions in DfosDN expression. We conclude that Dfos aids macrophage gb

237   invasion by increasing the mRNA levels of the filamin actin crosslinker Cher and the

238   tetraspanin TM4SF.

239   **Fig 3. Dfos regulates macrophage germband invasion through cytoskeletal regulators**
240   **the Filamin Cheerio and the tetraspanin TM4SF**

241   **(A)** Schematic representing the pipeline for analyzing mRNA levels in FACS sorted
242   macrophages.

243   **(B)** Table of genes down-regulated in macrophages expressing DfosDN. Genes are ordered
244   according to the normalized p-value from the RNA-Sequencing. The closest mouse protein
245   orthologs were found using UniProt BLAST; the hit with the top score is shown in the table.

246   **(C-F)** Lateral views of representative St 12 embryos in which the two targets with links to
247   actin organization, **(D)** the Tetraspanin TM4SF and **(E)** the Filamin Cheerio, have been
248   knocked down individually or **(F)** together, along with the control **(C)**. Scale bar: 50 μm.

249   **(G)** Quantification shows that the number of macrophages in the germband is reduced in
250   embryos expressing RNAi against either *cher (KK 107451)* or *TM4SF (KK 102206)* in
251   macrophages, and even more strongly affected in the double RNAi of both. Control vs. *cher*
252   *RNAi* p=0.0005 (46% reduction). Control vs. *TM4SF RNAi* p=0.009 (37% reduction), Control
253   vs. *cher/TM4SF RNAi* p>0.0001 (61% reduction). *cher RNAi* vs. *TM4SF RNAi* p=0.15.

254   **(H-K)** Lateral views of a representative St 12 embryo from **(H)** the control, as well as
255   embryos expressing DfosDN in macrophages along with either **(I)** GFP, **(J)** Cher, or **(K)**
256   TM4SF.

257   **(L)** Quantification shows that over-expression of TM4SF in DfosDN expressing
258   macrophages restores their normal numbers in the gb. Over-expression of Cher in this
259   background shows a strong trend towards rescue, but did not reach statistical significance.
260   Control vs. *DfosDN* p=0.015 (28% reduction); Control vs. *cher* p=0.74; Control vs. *TM4SF*

261 p>0.99; *DfosDN* vs. *DfosDN cher* p=0.14; DfosDN vs. *DfosDN, TM4SF* p<0.0001; Control

262 vs. *cher* p=0.97; Control vs. *TM4SF* p=0.35.

263 **(M-O)** q-PCR analysis of mRNA extracted from the bones of mice that are wild type,

264 transgenic (tg) for *Fos* controlled by a Major Histocompatibility promoter and viral 3'UTR

265 elements, and those in which such c-Fos transgenesis has led to an osteosarcoma (OS).

266 Analysis of mRNA expression shows that higher levels of **(M)** *Fos* correlate with higher

267 levels of **(N-N")** FlnA-C, and **(O)** Tspan6 in osteosarcomas. p values = 0.86, 0.001, 0.003 in

268 **M**, 0.98, 0.009, 0.007 in **N**, 0.39, < 0.0001, <0.0001 in **N'**, 0.76, 0.005, 0.002 in **N"**, 0.99,

269 0.004, 0.003 in **O**. Scale bar: 50 μm.

270 Macrophages are labeled using either **(C-F)** *srp::H2A::3xmCherry* or **(H-K)** *srpHemo-Gal4*

271 ("mac>") driving *UAS-mCherry::nls*. ***p<0.005, **p<0.01, *p<0.05. Unpaired t-test or

272 one-way ANOVA with Tukey post hoc were used for statistics. Each column contains the

273 number of analyzed embryos.

274 **In murine osteosarcoma c-fos mRNA level increases correlate with those of Filamins**

275 **and Tetraspanin-6**

276 To determine if these Dfos targets in *Drosophila* could also be Fos targets in vertebrate

277 cells, we utilized a well-established murine transgenic model that over expresses c-fos. In

278 these mice transgenic c-fos expression from viral 3' UTR elements in osteoblasts (the bone

279 forming cells) leads to osteosarcoma development accompanied by a 5 fold increase in c-fos

280 mRNA expression (Fig 3M) (Linder et al., 2018). We examined by qPCR the mRNA levels

281 of our identified Dfos targets' orthologs, comparing their levels in osteosarcomas (Fos tg

282 OS) to neighboring, osteoblast-containing healthy bones from Fos tg mice (Fos tg bone) and

283 control bones from wild-type mice (wt bone). We saw 2.5 to 8 fold higher mRNA levels of

284 the three murine Filamin orthologs (Fig 3N-N") and a 15 fold increase in Tetraspanin-6 (Fig

285 3O) in osteosarcoma cells. mRNA levels of several of the orthologs of other Dfos targets we

286 had identified showed less strong inductions or even decreases; the Glutathione S transferase

287 Gstt3 and the Slit receptor Eva1c increased 4 and 2.8 fold respectively, while the

288 mitochondrial translocator Tspo was 25% lower (S3F-I Fig). These results suggest that

289 Dfos's ability to increase mRNA levels of two key functional targets for migration, a

290 Filamin and a Tetraspanin, is maintained by at least one vertebrate fos family member.

291

292 **Dfos increases cortical actin polymerization through Cheerio and TM4SF to aid**

293 **macrophage invasion**

294 We wished to determine what cellular properties Dfos could affect through such targets to

295 facilitate *Drosophila* macrophage invasion. Given Cheerio's known role as an actin

296 crosslinker, we examined actin in invading *mac>DfosDN* macrophages within live embryos.

297 To visualize actin in macrophages, we utilized a *srpHemo-moe::3xmCherry* reporter which

298 marks cortical F-actin (Edwards et al., 1997; Franck et al., 1993) and observed a reduction of

299 53% (Fig 4A-D) in invading m*ac>DfosDN* macrophages. We hypothesized that these

300 changes in actin all around the cell edge could be due to the lower levels of Cheerio and/or

301 TM4SF mRNA in the *mac>DfosDN* macrophages. Indeed, we observed reductions in

302 *moe::3xmCherry* all around the edge of invading macrophages in live embryos expressing

303 RNAi against Cher or TM4SF in macrophages, (Fig 4E-H). To test if a decrease in actin

304 assembly could underlie the reduced tissue invasion of *mac>DfosDN* macrophages, we

305 forced cortical actin polymerization by expressing a constitutively active version of the

306 formin Diaphanous (Dia-CA) which localizes to the cortex (Gonzalez-Gaitan and Peifer,

307 2009). Indeed, Dia-CA completely rescued the *DfosDN* invasion defect (Fig 4I-J). Given that

308 Dia, like Dfos, does not affect general macrophage migratory capacities along the ventral

309 nerve cord (Davis et al., 2015), we examined if Dia might normally play a role in invasion.

310 We utilized two RNAis against Dia and observed decreased macrophage numbers in the gb in

311 each (Fig 4K-L) with no effect on numbers in the pre-gb (S4A Fig) or on the vnc (S4B Fig).

312 These results argue that Dfos aids invasion by increasing levels of TM4SF and Cheerio to

313   enhance actin polymerization around the surface of the macrophage, potentially by increasing

314   the activity of Dia.

315   **Fig 4. Dfos regulates the actin cytoskeleton through Cher, TM4SF, and the formin Diaphanous**

316   **(A)** Quantification of phalloidin intensity to detect F actin at the macrophage-macrophage contacts in

317   Stage 11/12 *Dfos[1]* embryos. F-actin is strongly reduced at these homotypic contacts.

318   **(B-C, F-H)** Representative confocal images of live embryos expressing in invading macrophages the

319   F-actin binding and homodimerizing portion of Moesin (*srpHemo-moe::3xmCherry)* to label F-actin.

320   Relative Moe-3xmCherry intensity is indicated with a pseudo-color heat map as indicated on the left,

321   with yellow as the highest levels and dark blue as the lowest.

322   **(D-E)** Quantification of the macrophage Moe:3xmCherry intensity as a measure of cortical F-actin,

323   normalized to the average fluorescence intensity of the control per batch.

324   **(D)** Quantification shows that macrophages expressing DfosDN display a 53% reduction in

325   Moe::3xmCherry intensity compared to the control when the two outliers shown as single dots are

326   excluded, 37% if they are included. Outliers identified by 10% ROUT. n of ROIs analysed = 650 for

327   control, 687 for *DfosDN*. p=0.0007 for analysis including outliers (Kolmogorov-Smirnov) and

328   p<0.0001 for analysis excluding outliers (Welch's t-test).

329   **(E)** Quantification reveals that macrophage expression of an RNAi against either *cher* or *TM4SF*, the

330   two genes whose expression is reduced in *DfosDN*, also results in a decrease of Moe::3xmCherry

331   intensity (by 40% each). n of ROIs analysed = 549 for control, 423 for *cher RNAi*, 306 for *TM4SF*

332   *RNAi*. Control vs. *cher RNAi* p=0.006. Control vs. *TM4SF* p=0.003.

333   **(I,I')** Representative confocal images of St 12 embryos from the control and a line in which

334   macrophages express DfosDN and a constitutively active (CA) form of the formin Dia to restore

335   cortical actin polymerization.

336   **(J)** Quantification shows that while macrophage expression of DiaCA does not significantly affect the

337   number of macrophages in the gb, expressing it in a DfosDN background rescues that lines'

338   macrophages gb invasion. Control vs. *DfosDN* p=0.017 (28% reduction), Control vs. *diaCA* p=0.18,

339   Control vs. *DfosDN, diaCA* p=0.010, *DfosDN* vs. *DfosDN, diaCA* p<0.0001

340   **(K,K')** Representative confocal images of St 12 embryos from the control and from a line expressing

341   an RNAi against *dia* in macrophages.

342   **(L)** Quantification of two RNAi lines against *dia* expressed in macrophages shows a 37% and 21%

343   reduction in macrophage numbers in the gb compared to control. Control vs. *dia RNAi[1]* (TRiP

344   HMS05027) p<0. 0001; control vs. *dia RNAi[2]* (TRiP HMS00308) p=0.0008.

345   Macrophages are labeled using either *srpHemo-Gal4* driving *UAS-mCherry::nls* (**I-I'**), or *srpHemo-*

346   *H2A::3xmCherry* (**K-K'**). *srpHemo-moe::3xmCherry*, *srpHemo-Gal4* crossed to (**B**) *UAS-GFP* as a

347   Control, (**C**) *UAS-DfosDN*, (**F**) w⁻ Control, (**G**) *UAS-cher RNAi* (KK 107451), or (**H**) *UAS-TM4SF*

348   *RNAi* (KK 102206). ***$p<0.005$, **$p<0.01$, *$p<0.05$. Unpaired t-test used for **A,** one way ANOVA

349   with Tukey post hoc for **E, J, L** and Welch's t test of normalized average mean intensity per embryo

350   for **D** with the two indicated outliers excluded, for statistical assessment. The number of analyzed (**A**)

351   macrophage-macrophage junctions, or (**D-E, J, L**) embryos is shown in each column. Scale bar 10 μm

352   in (**B-C, F-H**), 50 μm in (**I, K**).

353   We examined what consequence these lower cortical F-actin levels had on the cellular

354   behavior of macrophages during entry. Quantitation showed that the actin protrusion that

355   macrophages initially insert between the ectoderm and mesoderm during invasion was

356   actually longer in the *mac>DfosDN >*LifeAct::GFP macrophages than in the control (Fig 5A,

357   S5A Fig, S4 Movie). We then performed live imaging of macrophages labeled with

358   CLIP::GFP to visualize microtubules and thus cell outlines in both genotypes; we determined

359   the aspect ratio (maximal length over width) that the first entering cell displays as it enters

360   into the gb. The first DfosDN-expressing macrophage was extended even before it had fully

361   moved its rear into the gb (S5B Fig). We carried out measurements, taking only cells that had

362   entered the gb to be able to clearly distinguish the rear of the macrophage from following

363   cells (Fig 5B). We also avoided including in this measurement the forward protrusion and

364   determined that the first macrophage inside the gb displays an average increase of 23% in the

365   maximal length (L) of the cell body and a 12% reduction in the maximal width (W) (S5 Fig).

366   Interestingly, in the pre-gb zone the aspect ratio (max L/W) of *mac>DfosDN* macrophages

367   was not different from control macrophages (Fig 5C-D) although the *mac>DfosDN* cells

368   were 9% smaller in both their length and width (S5D Fig). This suggested that the gb could

369   impose resistance on the entering macrophage, an effect which *mac>DfosDN* macrophages

370   have trouble overcoming due to their compromised actin cytoskeleton at the cortex.

Belyaeva et al

Fig 5. Dfos aids macrophage gb invasion against the resistance of surrounding tissues and buffers the nucleus

(A) Quantification from live embryos shows that the length of the F-actin protrusion of the first entering macrophage is longer in macrophages expressing DfosDN. p= 0.011. The F-actin protrusion labelled with *srpHemo-Gal4* driving *UAS-LifeAct::GFP* was measured in the direction of forward migration (see schematic).

(B-C) Stills from 2-photon movies of St 11 embryos showing **(B)** the first macrophages entering the gb and **(C)** macrophages in the pre-gb zone in the control and in a line expressing DfosDN in macrophages. Microtubules are labelled with *srpHemo-Gal4* driving *UAS-CLIP::GFP*. A blue arrow indicates the front and a yellow arrow indicates the rear of the macrophage. Schematics above indicate where images were acquired

(D) Schematic at left shows macrophage measurements: vertical line for the maximum length and horizontal line for the maximum width. Histograms show the probability density distributions of the aspect ratios (maximum length over maximum width) of the first macrophage entering the gb (left) and macrophages in the pre-gb (right). Macrophages expressing *DfosDN* are more elongated the *mac>DfosDN* line. Control vs. *DfosDN* aspect ratios at gb entry p=0.0004, in pre-gb p=0.39.

Confocal images of St 12 embryos expressing RNAi against Lamin or LaminC in macrophages in **(E-E''')** the control, or **(F-F''')** in embryos also expressing DfosDN in macrophages. *srpHemo-GAL4* used as drover. *Lam RNAi[1]*: GD45636; *RNAi[2]*KK107419. *Lam C RNAi:* TRiP JF01406

 (G) Macrophage RNAi knockdown of Lamins which can increase nuclear deformability did not affect macrophages numbers in the gb in the control. In embryos in which macrophages expressed DfosDN, Lamin knockdown rescues their reduced numbers in the gb. Control vs. *DfosDN* p<0.0001. Control vs. *Lam RNAi[1]* p>0.99, vs. *Lam RNAi[2]* p=0.83, vs. *LamC RNAi* p>0.99. Control vs. *DfosDN, Lam RNAi[1]* p=0.024, vs. *DfosDN, Lam RNAi[2]* p>0.99, vs. *DfosDN, LamC RNAi* p>0.99. *DfosDN* vs. *DfosDN, Lam RNAi[1]* p<0.0001, vs. *DfosDN, Lam RNAi[2]* p=0.0049, vs. *DfosDN, LamC RNAi* p<0.0001.

(H) Expressing *DfosDN* in macrophages reduces their number in the gb. Concomitantly reducing tissue tension in the ectoderm (light blue in schematic) through Rho1DN substantially rescues invasion. *srpHemo-QF QUAS* control (*mac<>)* governed macrophage expression and *e22C-GAL4* ectodermal (*ecto>*). Control vs. *mac<>DfosDN* p<0.0001 (56% reduction), vs. *mac<>DfosDN; ecto>Rho1DN* p>0.99, vs. *ecto>Rho1DN* p=0.11. *mac<>DfosDN* vs. *mac<>DfosDN; ecto>Rho1DN* p<0.0001, vs. *ecto>Rho1DN* p=0.0044. *mac<>DfosDN; ecto>Rh1oDN* vs. *ecto>Rho1DN* p>0.99.

405 Macrophages are labeled in **B-C** by *srp-Gal4* driving *UAS-CLIP::GFP*, and in **E-F'''** by *srpHemo-*

406 *Gal4 UAS-mCherry-nls*. ***p<0.005, **p<0.01, *p<0.05. Unpaired t-test was used for **A,** one way

407 ANOVA with Tukey post hoc for **G, H**. The number shown within the column corresponds to

408 measurements in **A,** and analysed embryos in **G, H.** Scale bar 5μm in **B-C**, and 50μm in **E-F'''**.

409

410 **Dfos promotes advancement of macrophages against the resistance of the surrounding**

411 **tissues and buffers the nucleus**

412 We therefore examined how the properties of the gb tissues and macrophages interact during

413 invasion. We first investigated if the macrophage nucleus impedes normal invasion by

414 varying levels of the two *Drosophila* Lamin genes, Lam and LamC, both equally related to

415 the vertebrate lamins A and B1 (Muñoz-Alarcón et al., 2007) and both shown to affect

416 nuclear stiffness and deformability (Wintner et al., 2020; Zwerger et al., 2013). Over-

417 expressing Lam (S5E Fig) or knocking down either of these Lamins in macrophages

418 through RNAi (Perkins et al., 2015) did not change macrophage numbers in the gb of wild

419 type embryos (Fig 5E-E''', G), suggesting that the stiffness of the macrophage nucleus is

420 not a rate limiting parameter during normal tissue invasion into the narrow path between the

421 ectoderm and mesoderm, This result also argues that Lamins' capacity to alter gene

422 expression is not normally important for invasion (Andrés & González, 2009). However in

423 *mac>DfosDN* macrophages, knockdown of these Lamins was able to rescue the gb invasion

424 defect (Fig 5E-G), supporting the conclusion that the properties of the nucleus affect

425 invasion in the absence of the higher levels of cortical actin Dfos normally induces. To

426 directly test if reducing the tension of surrounding tissues can counteract the absence of

427 Dfos, we expressed Rho1DN in the ectoderm with the *e22C-GAL4* driver while expressing

428 *QUAS-DfosDN* in macrophages with the GAL4-independent Q-system driver we had

429 constructed, *srpHemo-QF2* (Gyoergy et al., 2018). Rho1 through ROCK is a key regulator

430 of Myosin activity, epithelial tension and tissue stiffness (Warner & Longmore, 2009; Zhou

431 et al., 2009); Myosin II is essential for actin contractility (Heer & Martin, 2017) and tension

Belyaeva et al

432   in the *Drosophila* gb ectoderm (Ratheesh et al., 2018). Indeed, we found that this reduction

433   of ectodermal tension substantially rescued DfosDN expressing macrophage numbers in the

434   gb (Fig 5H). Taken together our results argue that Dfos aids *Drosophila* macrophages in

435   withstanding the resisting force of surrounding cells against the nucleus during invasion into

436   tissues.

437

438   **Discussion:**

439   We identify the ability to tune the state of the cortical actin cytoskeleton as a key

440   capacity for immune cells migrating into and within tissue barriers *in vivo*. We find that

441   macrophages upregulate a program governed by the transcription factor Dfos to enable this.

442   Dfos in *Drosophila* is known to regulate the movement during dorsal or wound closure of

443   epithelial sheets (Brock et al., 2012; Lesch et al., 2010; Riesgo-Escovar & Hafen, 1997;

444   Zeitlinger et al., 1997) as well as the development of epithelial tumors and their

445   dissemination (Külshammer et al., 2015; Uhlirova & Bohmann, 2006; Külshammer &

446   Uhlirova, 2013; Benhra et al., 2018). Here we define a different role, namely that Dfos

447   enables a stream of individual immune cells to efficiently push their way into tissues, a

448   process which is aided rather than hampered by the presence of the ECM (Sánchez-Sánchez

449   et al., 2017; Valoskova et al., 2019). This function appears specifically required for invasion

450   as we observe no defects in *DfosDN* macrophages' migratory speed in open environments.

451   *DfosDN* macrophages display decreased actin at the cell edge and an elongated shape within

452   the germband, suggesting a defect in the stiffness of the cortex. Indeed, only in the presence

453   of *DfosDN* does the state of the nucleus become relevant, with reductions in Lamins shown

454   to underlie nuclear stiffness (Wintner et al., 2020) enhancing the ability of macrophages to

455   invade. These findings along with the ability of a softened ectoderm to substantially rescue

456   the *DfosDN* macrophages' germband invasion defect lead us to propose the model (Fig 6)

457   that Dfos permits efficient initial translocation of the macrophage body under ectodermal

458   reactive load by forming a stiff cortical actin shell that counteracts surrounding tissue

459   resistance and protects the nucleus from undergoing high levels of mechanical stress during

460   its deformation.

461   **Fig. 6. Model: Dfos increases actin assembly and crosslinking through the tetraspanin TM4SF**

462   **and the Filamin Cheerio to counter surrounding tissue resistance**

463   We propose a model for how Dfos tunes the cortical actin properties of *Drosophila* embryonic
464   macrophages to aid their infiltration against the resistance of the surrounding germband tissue. Dfos
465   leads to an increase of the tetraspanin TM4SF and the Filamin Cheerio (Cher). The binding of TM4SF
466   and Filamin to different partners (see Figure S6) forms a network at the cell surface of Integrin, actin
467   and upstream signaling molecules; this results in the recruitment of Rho GEFs and activation of Rho
468   GTPases and the formin Diaphanous, which can stimulate further actin polymerization. Thereby, F-
469   actin is assembled into a more crosslinked and dense network aiding the macrophage in moving its
470   cell body into the ecto-meso interface. The presence of Lamin around the nuclear membrane does not
471   affect this process in the wildtype. However, in the DfosDN-expressing macrophages, the loss of Cher
472   and TM4SF lead to reduced cross-linked actin levels at the cell cortex making the stiffness of the
473   nucleus the rate limiting step for macrophage infiltration of the gb tissue.

474   **A molecular program for tissue invasion that strengthens cortical actin**

475   Crucial mediators of this process are two actin regulators, the filamin Cher, known to

476   be a Dfos target in epithelia, and the previously uncharacterized membrane scaffold

477   tetraspanin TM4SF. We show that both require Dfos for higher mRNA levels in

478   macrophages and present correlative evidence that these classes of genes are also

479   upregulated by vertebrate c-fos. Each of these Dfos targets is required for macrophage

480   invasion; over-expression of TM4SF in macrophages can rescue the *DfosDN* tissue invasion

481   phenotype. We propose that these targets act together to tune the actin cytoskeleton for

482   tissue invasion. Higher Filamin levels cross-link actin filaments into resilient and stiffer

483   networks maintaining cell integrity during mechanical stress (Goldmann et al., 1997; Tseng

484   et al., 2004; Fujita et al., 2012). This aids the distribution of forces from focal adhesions

18

485 across the entire migrating cell body, since Filamins can bind directly to Integrin, and even

486 more strongly under strain (Ehrlicher et al., 2011; Glogauer et al., 1998; Kumar et al., 2019;

487 Razinia et al., 2012). Tetraspanins, self-associating multipass transmembrane proteins, also

488 can bind Integrin, forming microdomains of adhesion molecules, receptors and their

489 intracellular signaling complexes, including Rho GTPases (Zimmerman, et al., 2016;

490 Termini & Gillette, 2017; Yáñez-Mó et al., 2009; Berditchevski & Odintsova, 1999).

491 Filamins similarly bind receptors, regulators of actin assembly, Rho GTPases and the Rho

492 GEF Trio (Popowicz et al., 2006; Stossel et al., 2001; Vadlamudi et al., 2002; Ohta et al.,

493 1999; Bellanger et al., 2000). Given that we observe reduced macrophage cortical F-actin in

494 the absence of either the Filamin Cheerio or the Tetraspanin TM4SF we propose that these

495 targets enhance the recruitment and activation of Rho GTPases and the formin Dia to

496 stimulate actin polymerization (Fig 6, S6 Fig) (Rousso et al., 2013; Seth et al., 2006;

497 Großhans et al., 2005; Williams et al., 2007; Delaguillaumie et al., 2002). Dfos'

498 upregulation of both targets could thus lead to a supra-network in which ECM-anchored FAs

499 connect to a strong cross-linked cortical actin lattice, allowing Myosin contraction to be

500 converted into cellular advancement despite resistance from the flanking ectoderm.

501   We demonstrate that the actin nucleating formin Dia is important for *Drosophila*

502 macrophage invasion and capable of rescuing the defects in the *DfosDN* mutant. Unlike the

503 formin Ena which mediates chemotaxis (Davidson et al., 2019), Dia is not required for

504 general *Drosophila* macrophage migration, and instead allows macrophages to recoil away

505 from one another (Davis et al., 2015). Dia could be required for macrophages specifically

506 when they face resistance from their surroundings. Modeling indicates that Dia1's regulation

507 of cortical tension requires an optimal combination of actin cross linking and intermediate

508 actin filament length (Chugh et al., 2017). *Drosophila* Dia is a more processive nucleator

509 than Ena (Bilancia et al., 2014) and thus could create the intermediate length actin filaments

Belyaeva et al

510   that enable higher levels of macrophage cortical tension and strain stiffening (Kasza et al.,

511   2010) on all sides of the cell during their invasion.

512   Our findings thus demonstrate that there are commonalities in the molecular

513   mechanisms by which *Drosophila* cells invade into either confluent tissues or the ECM.

514   Dfos's upregulation of the Filamin Cheerio is also required in tumor cells and aneuploid

515   epithelial cells to enhance ECM breaching (Külshammer & Uhlirova, 2013; Benhra et al.,

516   2018). Both cell types displayed enhanced levels of cortical filamentous actin, which in the

517   tumors is concomitant with Dia upregulation (Külshammer & Uhlirova, 2013). In the

518   oocyte, Filamin is required for follicle cell intercalation and border cells display higher

519   levels of Filamin and F-actin to maintain cellular integrity during migration between nurse

520   cells (Sokol & Cooley, 2003; Somogyi & Rørth, 2004). The mediator of these increased F-

521   actin levels, MAL-D, can be activated by Dia (Somogyi & Rørth, 2004). Thus while MMPs

522   may be specific to ECM crossing, a denser and more cross linked actin cortex due to

523   increased levels of the filamin Cheerio and activity of the formin Dia could be a common

524   feature of *Drosophila* cells moving through the resistance of either ECM or surrounding

525   tissues. Determining if such shifts in cell surface actin properties underlie some cancer cells'

526   capacity to metastasize even in the presence of MMP inhibitors is an interesting area of

527   inquiry (Butcher et al 2009; Kessenbrock et al 2010).

528

529   **Implications for vertebrate immune cell migration**

530   Our work also suggests a new perspective on the migration of some vertebrate

531   immune cells. We find that altering lamin levels does not normally affect *Drosophila*

532   macrophage tissue invasion. This contrasts with results showing that nuclear deformability

533   from lower lamin levels underlies the migration of some immune cell types through narrow

534   constrictions engineered from rigid materials (Davidson et al., 2014; Thiam et al, 2016).

535 However, negotiation of such extremely challenging *in vitro* environments can lead to DNA

536 damage (Raab et al., 2016) and higher nuclear flexibility caused by lower lamin levels is

537 associated with increased cell death (Harada et al., 2014). A robust cell surface actin layer

538 would allow long-lived cells or those not easily replenished to protect their genome as they

539 move through resistant yet deformable environment. Embryonic *Drosophila* and vertebrate

540 tissue resident macrophages migrate into tissues during development, survive into the adult,

541 and serve as founders of proliferative hematopoetic niches (Holz et al., 2003; Makhijani et

542 al., 2011; Bosch et al., 2019; Ginhoux and Guilliams, 2016; Theret et al 2019; Guilliams et

543 al, 2020). Tissue resident memory T cells migrate in response to infection in mature animals,

544 are long-lived and not easily renewed from the blood (Szabo et al., 2019). Thus the

545 importance of nuclear mechanics for migration in challenging *in vivo* environments should

546 be explored for a broader range of immune cells as well as the utilization of cortical actin as

547 a strategy for genomic protection.

548

549

Materials and Methods

550

Fly strains and genetics

551

552 Flies were raised on standard food bought from IMBA (Vienna, Austria) containing agar,

553 cornmeal, and molasses with the addition of 1.5% Nipagin. Adults were placed in cages in a

554 fly room or a Percival DR36VL incubator maintained at 25ºC and 65% humidity or a Sanyo

555 MIR-153 incubator at 29ºC within the humidity controlled 25ºC fly room; embryos were

556 collected on standard plates prepared in house from apple juice, sugar, agar and Nipagin

557 supplemented with yeast from Lesaffre (Marcq, France) on the plate surface. Fly crosses and

558 embryo collections for RNA interference experiments (7 hour collection) as well as live

559   imaging (6 hour collection) were conducted at 29ºC to optimize expression under GAL4

560   driver control (Duffy, 2002). All fly lines utilized are listed below.

561

562   **Fly stocks**

563   *srpHemo-GAL4 (mac>)* was provided by K. Brückner (UCSF, USA)(Brückner et al., 2004).

564   *Oregon R (control), P{CaryP}attP2 (control), P{CaryP}attP40 (control), kay² (Dfos²),*

565   *(UAS-Fra)2 (Dfos), UAS-Rho1.N19 Rho1DN), UAS-fbz (DfosDN), UAS-kayak* RNAi *(Dfos*

566   *RNAi)* TRiP HMS00254 and TRiP JF02804, *UAS-dia RNAi* TRiP HM05027, *UAS-LamC*

567   *RNAi* TRiP JF01406 and TRiP HMS00308, *e22c-GAL4 (ecto>), Resille::GFP, UAS-*

568   *GFP.nls, UAS-mCherry.nls, UAS-CD8::GFP* lines were obtained from the Bloomington

569   Stock Center (Indiana, USA). *kay¹ (Dfos¹)* line was provided by O. Schuldiner (WIS, Israel).

570   *UAS-dia.deltaDad.EGFP (diaCA)* and *srpHemo-GAL4 UAS-CLIP::GFP*

571   *(mac>CLIP::GFP)* lines were provided by B. Stramer (KCL, UK). *UAS-cher.FLAG (cher)*

572   line was provided by M. Uhlirova (CECAD, Germany). *w[1118] (control), UAS-cher* RNAi

573   KK107451, *UAS-TM4SF* RNAi KK102206, *UAS-Lam RNAi¹* GD45636, *UAS-Lam RNAi²*

574   KK107419 lines were obtained from the Vienna *Drosophila* Resource Center (Austria).

575   **Extended genotypes:**

576   Here we list the lines used in each Fig; we state first the name from FlyBase; in parentheses

577   the name used in the Fig panels is provided.

578   **Fig 1 and S1 Fig:**

579   Fig 1D: *Oregon R.* Fig 1E-G and S1A Fig: *srpHemo-GAL4, UAS-GFP (control).* Fig 1H:

580   *srpHemo-GAL4, UAS-GFP; kay¹ (Dfos¹).* Fig 1I-L and S1B, G Fig: *srpHemo-GAL4, UAS-*

581   *GFP.nls/+ (control 1).* Fig 1H, 1J, 1N: *srpHemo-GAL4, UAS-GFP/+; kay¹ (Dfos¹).* Fig 1K, 1N

582   and S1B Fig: *srpHemo-GAL4, UAS-GFP.nls/+; kay² (Dfos²)* Fig 1L, 1N: *srpHemo-GAL4, UAS-*

583   *GFP.nls/(UAS-Fra)2; kay² (Dfos²;mac>Dfos).* Fig 1O, 1Q and S1C-E Fig: *srpHemo-Gal4,*

584   *srpHemo-H2A::3xmCherry/+ (control 2)*. Fig 1P-Q and S1C-E Fig: *srpHemo-Gal4, srpHemo-*

585   *H2A::3xmCherry/UAS-fbz (mac>DfosDN)*. Fig 1R and S1F Fig: *srpHemo-GAL4, UAS-GFP,*

586   *UAS-H2A::RFP/ P{CaryP}attP2 (control)*. Fig 1R and S1F Fig: *srpHemo-GAL4, UAS-GFP,*

587   *UAS-H2A::RFP /UAS-kayak* RNAi HMS00254 and JF02804 (*mac>Dfos RNAi[1], mac>Dfos*

588   *RNAi[2]*). S1G Fig: *srpHemo-GAL4, UAS-GFP.nls/(UAS-Fra)2 (mac>Dfos)*.

589   **Fig 2 and S2 Fig:**

590   Fig 2A, 2C-I and S2A-B, E Fig: *srpHemo-Gal4, srpHemo-H2A::3xmCherry/+ (control)*. Fig

591   2D: *srpHemo-Gal4, srpHemo-H2A::3xmCherry/+* (3 movies) and *Resille::GFP/+; srpHemo-*

592   *Gal4, srpHemo-H2A::3xmCherry/+* (4 movies, control) and *Resille::GFP/+; srpHemo-Gal4,*

593   *srpHemo-H2A::3xmCherry/+* (3 movies) and *Resille::GFP/+; srpHemo-Gal4, srpHemo-*

594   *H2A::3xmCherry/UAS-DfosDN (*4 movies, *DfosDN)* Fig 2A, 2C-I and S2A-B, E Fig: *srpHemo-*

595   *Gal4, srpHemo-H2A::3xmCherry/UAS-fbz (mac>DfosDN)*. S2C-D Fig: *srpHemo-GAL4, UAS-*

596   *GFP.nls/+ (control)*. S2C-D Fig: *srpHemo-GAL4, UAS-GFP.nls/+; kay[2] (Dfos[2])*.

597   **Fig 3 and S3 Fig:**

598   Fig 3C, G and S3D Fig: *UASDicer2;; srpHemo-Gal4, srpHemo-H2A::3xmCherry/w[1118]*

599   *(control)*. Fig 3D, 3G and S3D Fig: *UASDicer2; UAS-TM4SF RNAi* KK10220/+; *srpHemo-*

600   *Gal4, srpHemo-H2A::3xmCherry/+ (mac>TM4SF RNAi)*. Fig 3E, G and S3D Fig:

601   *UASDicer2; UAS-cher RNAi* KK107451/+; *srpHemo-Gal4, srpHemo-H2A::3xmCherry/+*

602   *(mac>cher RNAi)*. Fig 3F-G: *UAS-Dicer2;UAS-cher RNAi* KK107451/*UAS-TM4SF RNAi*

603   KK102206; *srpHemo-Gal4, srpHemo-H2A::3xmCherry/+ (mac>TM4SF RNAi, cher RNAi)*.

604   Fig 3H, L: *srpHemo-GAL4, UAS-mCherry.nls/UAS-mCD8::GFP (control)*. Fig 3I, L:

605   *srpHemo-GAL4, UAS-mCherry.nls/UAS-mCD8::GFP; UAS-fbz/+ (mac>DfosDN)*. Fig 3J,

606   L: *srpHemo-GAL4,UAS-mCherry.nls/UAS-cheerio.FLAG; UAS-fbz/+ (mac>DfosDN, cher)*.

607   Fig 3K-L: *srpHemo-GAL4,UAS-mCherry.nls/UAS-TM4SF; UAS-fbz/+ (mac>DfosDN,*

608   *TM4SF)*. Fig 3L: *srpHemo-GAL4, UAS-mCherry.nls/ UAS-TM4SF (mac>TM4SF)*. Fig 3L:

609   *srpHemo-GAL4, UAS-mCherry.nls/ UAS-cher (mac>cher).* S3A-C Fig: *srpHemo-Gal4,*

610   *srpHemo-3xmCherry/+ (control).* S3A-C Fig: *srpHemo-Gal4, srpHemo-3xmCherry/UAS-fbz*

611   *(mac>DfosDN).*

612   **Fig 4 and S4 Fig:**

613   Fig 4B, D: *srpHemo-Gal4, srpHemo-moe::3xmCherry/+;UAS-mCD8::GFP/+*

614   *(Control).* Fig 4C-D: *srpHemo-Gal4, srpHemo-moe::3xmCherry/UAS-fbz (mac>DfosDN).*

615   Fig 4E-F: *srpHemo-Gal4, srpHemo-moe::3xmCherry/w118 (Control).* Fig 4E, G: *srpHemo-*

616   *Gal4, srpHemo-moe::3xmCherry/UAS>cher*

617   *RNAi* KK107451 *(mac>cher RNAi).* Fig 4E, H: *srpHemo-*

618   *moe::3xmCherry/UAS>TM4SF RNAi* KK102206 *(mac>TM4SF RNAi).* Fig 4I-J: *srpHemo-*

619   *GAL4, UAS-mCherry.nls/UAS-mCD8::GFP (control).* Fig 4I', J:

620   *srpHemo-GAL4, UAS-mCherry.nls/UAS-Dia.deltaDad.EGFP; UAS-fbz/+ (mac>*

621   *DfosDN, diaCA).* Fig 4J: *srpHemo-GAL4, UAS-mCherry.nls/UAS-mCD8::GFP; UAS-fbz/+*

622   *(mac>DfosDN).* Fig 4J: *srpHemo-GAL4, UAS-mCherry.nls/ UAS-Dia.deltaDad.EGFP*

623   *(mac>diaCA).* Fig 4K-L and S4B-C Fig: *UASDicer2;; srpHemo-Gal4, srpHemo-*

624   *H2A::3xmCherry/P{CaryP}attP40 (control).* Fig 4K', L and S4B-C Fig: *UASDicer2;+;*

625   *srpHemo-Gal4, srpHemo-H2A::3xmCherry/ UAS-dia RNAi* HM05027 *(mac>dia RNAi[1]).* Fig

626   4L and S4B-C Fig: *UASDicer2;+; srpHemo-Gal4, srpHemo-H2A::3xmCherry/UAS-dia*

627   *RNAi* HMS00308 *(mac>dia RNAi[2]).*

628   **Fig 5 and S5 Fig:**

629   Fig 5A and S5A Fig: *srpHemo-Gal4 UAS-LifeActGFP UAS-RedStinger/ srpHemo-Gal4*

630   *UAS-LifeActGFP, UAS-RedStinger* control*; srpHemo-Gal4 UAS-LifeActGFP UAS-*

631   *RedStinger/ srpHemo-Gal4 UAS-LifeActGFP UAS-RedStinger; UAS-DfosDN/UAS-DfosDN.*

632   Fig 5B-D and S5B-D Fig: *srpHemo-Gal4, UAS-CLIP::GFP, UAS-RedStinger (control).* Fig

633   5B-D and S5B-D Fig: *srpHemo-Gal4, UAS-CLIP::GFP, UAS-RedStinger; UAS-fbz*

634   *(mac>DfosDN)*. Fig 5E, G: *srpHemo-GAL4, UAS-mCherry.nls/UAS-mCD8::GFP (control)*.

635   Fig 5E'-E'', 5G: *srpHemo-GAL4, UAS-mCherry.nls/UAS-Lamin RNAi GD45636,*

636   KK107419 *(mac>Lam RNAi[1] and mac>Lam RNAi[2], respectively)*. Fig 5E''', G: *srpHemo-*

637   *GAL4, UAS-mCherry.nls/UAS-LaminC RNAi TRIP JF01406 (mac>LamC RNAi)*. Fig 5F-G:

638   *srpHemo-GAL4, UAS-mCherry.nls/UAS-mCD8::GFP; UAS-fbz/+ (mac>DfosDN)*. Fig

639   5F',F'', G: *srpHemo-GAL4, UAS-mCherry.nls/UAS-Lam RNAi (Lam RNAi[1]=GD45636, Lam*

640   *RNAi[2]=KK107419); UAS-fbz/+ (mac>DfosDN, Lam RNAi[1] and mac>DfosDN, Lam RNAi[2])*.

641   Fig 5F''', G: *srpHemo-GAL4, UAS-mCherry.nls/UAS-LaminC RNAi TRIP JF01406; UAS-*

642   *fbz/+ (mac>DfosDN, LamC RNAi)*. Fig 5H: *e22CGal4,srpHemo-H2A::3xmCherry/+*

643   *(control)*. Fig 5H: *srpQF/ srpHemo-H2A::3xmCherry; QUAS-fbz/UAS-Rho1.N12*

644   *(mac<>DfosDN)*. Fig 5H: *e22CGal4, srpHemo-H2A::3xmCherry/srpQF; +/ UAS-Rho1.N12*

645   *(ecto>Rho1DN)*. Fig 5H: *srpQF/ e22C-Gal4, srpHemo-H2A::3xmCherry; UAS-*

646   *Rho1N12/QUAS-fbz (mac<>DfosDN, ecto>rhoDN)*. S5E Fig: *+;UAS-GFP::nls, srpHemo-*

647   *GAL4 (control). +;UAS-GFP::Lamin, srpHemo-GAL4.*

648

649   **Cloning and generation of QUAS-DfosDN line**

650   The fragment was amplified from genomic DNA of the published *UAS-fbz (UAS-Dfos DN)*

651   line (Eresh, Riese, Jackson, Bohmann, & Bienz, 1997) using primers encompassing a 5'

652   consensus translation initiation sequence followed by the bZIP fragment and containing

653   BglII and XhoI restriction sites: 5'-GAAGATCTATTGGGAATTCAACATGACCCCG-3'

654   and 5'-CCCTCGAGTCAGGTGACCACGCTCAGCAT-3'. The resulting fragment was

655   cloned into the pQUASt vector, a gift from Christopher Potter (Addgene plasmid # 104880).

656   The final construct was sequenced and injected into the attP2 landing site by BestGene

657   (Chino Hills, CA, USA).

658

Belyaeva et al

659 **Cloning and generation of UAS-TM4SF line**

660 The TM4SF open reading frame was amplified from the DGRC GH07902 cDNA clone

661 (#3260, Fbcl0121651), using primers acagcgGAATTCATGGCATTGCCGAAGAAAAT

662 and acagcgTCTAGATTAAAAGCTAATCGTCTGTCATT. The PCR product and the

663 pUASt-aTTB vector (DGRC plasmid #1419) were digested with EcoRI and XbaI, and

664 ligated. After sequencing, the construct was injected into the landing site line, (y^1 *M{vas-*

665 *int.Dm}ZH-2A w**; *M{3xP3-RFP.attP}ZH-51D*, BL 24483), to produce second chromosome

666 inserts. All male survivors were crossed to *w*; *Sp/CyO*; *PrDr/TM3Ser* virgins. Transformants

667 were recognized by eye color and crossed again to *w*; *Sp/CyO*; *PrDr/TM3Ser* virgins to get

668 rid of the X chromosomal integrase.

669

670 **Embryo staging:**

671 Laterally oriented embryos with complete germband (gb) extension and the presence of

672 stomadeal invagination were staged based on gb retraction from the anterior as a percentage

673 of total embryo length. Embryos with no gb retraction were classified as Stage 11, 30%

674 retraction early Stage 12, 60% retraction Stage 12, and 70% Stage 13. Imaged embryos are

675 shown throughout paper in a lateral orientation with anterior to the left and dorsal up.

676

677 *In situ* **hybridization and immunofluorescence**

678 Embryos were fixed with 3.7% formaldehyde/heptane for 20 min followed by methanol

679 devitellinization for *in situ* hybridization and visualization of 3xmCherry. The *Dfos* cDNA

680 clone SD04477 was obtained from the DGRC. T7 or T3 polymerase-synthesized

681 digoxigenin-labelled anti-sense probe preparation and *in situ* hybridization was performed

682 using standard methods (Lehmann & Tautz, 1994). Images were taken with a Nikon-Eclipse

683 Wide field microscope with a 20X 0.5 NA DIC water Immersion Objective. Embryos were

26

684   mounted after immunolabeling in Vectashield Mounting Medium (Vector Labs, Burlingame,

685   USA) and imaged with a Zeiss Inverted LSM700 and LSM800 Confocal Microscope using a

686   Plain-Apochromat 20X/0.8 Air Objective or a Plain-Apochromat 63X/1.4 Oil Objective as

687   required.

Antibody	Source animal	Dilution	Provided by
Anti-Dfos	Rabbit	1:50	J. Zeitlinger (Stowers Institute, USA)
Anti-GFP	Chicken	1:500	Abcam (ab13970)
Anti-mCherry	Goat	1:200	Invitrogen (M11217)

688

Dfos antibody

690   The Dfos rabbit polyclonal antibody was produced for the lab of Julia Zeitlinger. It was

691   raised by Genescript (Piscataway, NJ, USA) against the C-terminal end of *Drosophila* Kayak

692   found in all isoforms and was purified against an N terminally His tagged antigen

693   corresponding to aa 73 to 595 of Kay isoform A. The internal Genescript order number is

694   163185-30, and in the Zeitlinger lab is referred to as anti-kay/fos Ab.

695

Time-Lapse Imaging

697   Embryos were dechorionated in 50% bleach for 5 min, washed with water, and mounted in

698   halocarbon oil 27 (Sigma) on a 24x50mm high precision coverslip (Marienfeld Laboratory

699   Glassware, No. 1.5H) between two bridges (~0.5 cm high) of coverslips glued on top of

700   each other, or mounted in halocarbon oil 27 (Sigma) between a 18x18mm coverslip

701   (Marienfeld Laboratory Glassware, No. 1.5H) and an oxygen permeable membrane (YSI).

702   The embryo was imaged on an upright multiphoton microscope (TrimScope, LaVision)

703   equipped with a W Plan-Apochromat 40X/1.4 oil immersion objective (Olympus). GFP and

704   mCherry were imaged at 860 nm and 1100 nm excitation wavelengths, respectively, using a

705   Ti-Sapphire femtosecond laser system (Coherent Chameleon Ultra) combined with optical

706   parametric oscillator technology (Coherent Chameleon Compact OPO). Excitation intensity

707   profiles were adjusted to tissue penetration depth and Z-sectioning for imaging was set at

708   1μm for tracking. For long-term imaging, movies were acquired for 60 - 150 minutes with a

709   frame rate of 25-45 seconds. A temperature control unit set to 29°C was utilized for all

710   genotypes except kay^2 for which the setting was 25°C.

711

712   **Image Analysis**

713   **Macrophage cell counts:** Autofluorescence of the embryo revealed the position of the

714   germband (gb) for staging of fixed samples. Embryos with 40% (±5%) gb retraction (Stage

715   12) were analysed for macrophage numbers in the pre-gb, within the germband, along the

716   ventral nerve cord (vnc) and in the whole embryo. For the *kay RNAi*.embryos with 70% gb

717   retraction (Stage 13) were used for vnc counts. The pre-gb zone was defined based on

718   embryo and yolk autofluorescence as an area on the yolk sac underneath the amnioserosa

719   with borders defined posteriorly by the gb ectoderm and anteriorly by the head.

720   Macrophages were visualized using confocal microscopy with a Z-stack step size of 2 μm

721   and macrophage numbers within the gb or the segments of the vnc were calculated in

722   individual slices (and then aggregated) using the Cell Counter plugin in FIJI. Total

723   macrophage numbers were obtained using Imaris (Bitplane) by detecting all the macrophage

724   nuclei as spots.

725

726   **Macrophage Tracking, Speed, Persistence. Mode of Migration and Macrophage gb**

727   **crossing Analysis**

728   Embryos with macrophage nuclei labelled with *srpHemo-H2A::3XmCherry* and the

729   surrounding tissues with *Resille::GFP,* or with only macrophages labelled by *srpHemo-*

730   *H2A::3XmCherry, or srpHemo>GFP.nls* were imaged and 250x250x40μm³ 3D-stacks were

731   typically acquired with ~0.2x0.2x1μm³ voxel size every 39-41 seconds for ~2 hours. For

732   imaging macrophages on vnc frames were acquired at every 40-43 seconds for 30 min after

733   macrophages started spreading into abdominal segment 2 (see Fig 2G). Multiphoton

734   microscopy images were initially processed with ImSpector software (LaVision Bio Tec) to

735   compile channels, and exported files were further processed using Imaris software (Bitplane)

736   for 3D visualization.

737   Each movie was rotated and aligned along the embryonic AP axis for tracking analysis. For

738   analysis of migration in the pre-gb and gb in the control and *kay²* mutant, embryos were

739   synchronized using the onset of germ and retraction. For vnc migration analysis,

740   macrophages were tracked for 30 minutes from when macrophages started moving into the

741   second abdominal segment. Only macrophages migrating along the inner edge of the vnc

742   were analyzed.

743   Gb crossing time was calculated from when the macrophages align in front of the gb

744   ectoderm in a characteristic arc, until the first macrophage had transitioned its nucleus inside

745   the ecto-meso-interphase. To see the gb edge and yolk in movies of *srpHemo-*

746   *3xH2A::mCherry*, either *Resille::GFP* labelling the outlines of all cells, or the auto-

747   fluorescence of the yolk was used.

748   For analysis of gb migration in the *DfosDN* vs control macrophages, macrophages were

749   tracked from when the first macrophage appeared between the ectoderm and the yolk sac

750   until gb retraction started, typically 60 minutes. In the head and pre-gb, macrophage nuclei

751   were extracted using the spot detection function, and tracks generated in 3D over time. The

752   pre-gb and gb were defined as for macrophage counts described above. The mean position

753   of the tracks in X- and Y restrict analysis to each migratory zones.

754   Cell speed and persistence were calculated from nuclei positions using custom Python

755   scripts as described elsewhere (Smutny et al., 2017). Briefly, instantaneous velocities from

756   single cell trajectories were averaged to obtain a mean instantaneous velocity value over the

757   course of measurement. The directional persistence of a trajectory was calculated as the

758   mean cosine of an angle between subsequent instantaneous velocities:

759

$$I\left(v_1, \dots, v_l\right) = \frac{1}{l-1} \sum_{k=1}^{l-1} \cos(v_k, v_{k+1}),$$

760   where l is duration of the trajectory and $v_1, \dots, v_l$ are its instantaneous velocities. Only

761   trajectories with a minimal duration of 15 timeframes were used. Calculated persistence

762   values were averaged over all trajectories to obtain a persistence index (I) for the duration

763   of measurement (with -1 being the lowest and 1 the maximum). 3-6 embryos were

764   recorded and analyzed for each genotype, numbers of control and perturbed embryos are

765   equal in each pairwise comparison.

766

767   **Measurement of junctional Phalloidin**

768   The junctional intensity of F-actin (Phalloidin) was calculated using linescan analysis as

769   previously described (Smutny et al., 2010) with the following changes. The line was ~5 μm

770   and was always drawn in the middle slice of the Z stack (1 μm resolution) of the

771   macrophage-macrophage junction. For every line, a Gaussian fit was applied and maximum

772   intensities across the cell junction were then normalized against average intensities of F-

773   actin (Phalloidin) staining in the stereotypical gb area of ~50x50μm^2 in each embryo.

774   Analyses were carried out using standard Fiji software. 4-5 embryos were analysed per

775   genotype. Macrophages in the pre-gb or gb entry zones were analyzed.

776

777   **Measurement of F-actin reporters**

778   To quantify cortical F-actin intensity in living embryos, a *srpHemo-moe::3xmCherry*

779   reporter line (Gyoergy et al., 2018) was crossed into a background of macrophages

780   expressing *DfosDN*, *cher RNAi*, or *TM4SF* RNAi. Embryos were collected for 5h 30min at

781   29°C, de-chorionated in 50% bleach for 5 min, rinsed thoroughly with water, and aligned

782   laterally side by side under a stereomicroscope using a fluorescence lamp to check for the

783   presence of mCherry. Aligned embryos were then mounted as described in the live imaging

784   section above. To image Moe::3xmCherry, a Zeiss LSM800 inverted microscope was used

785   with the following settings: Plan-APOCHROMAT 40x/1.4 Oil, DIC, WD=0.13 objective,

786   1.5x zoom, 1025x1025 pixel, speed 8, heating chamber set to 29°C, z-interval 1μm. Laser

787   settings were kept constant in all experiments. Images were acquired during macrophage

788   invasion into the gb (St 12). Pseudo-coloring was conducted for the mCherry red channel.

789   Each pixel in the image has a color ascribed to it via the fire "Look Up Table" translating the

790   level of intensity of the mCherry channel into a defined amount of each color. The highest

791   intensity of the image is represented as very bright yellow and all other grey values are

792   depicted as colors on the scale accordingly.

793   For quantification of Moe::3xmCherry intensity, an ROI was drawn in Fiji software

794   around macrophages at the germband entry site in 20 z-stacks for each embryo. The area

795   mean intensity was measured in all ROIs and the average/embryo was calculated. To

796   normalize fluorescence intensities per batch, the average intensity/embryo of all ROIs in

797   each sample was divided by the arithmetic mean of the average intensity/embryo of all ROIs

798   in the control per batch. The normalized average intensities/embryo were then compared to

799   each other using a t-test with Welch's correction for *DfosDN* and one way-ANOVA for *cher*

800   *RNAi* and *TM4SF RNAi*.

801   **Cell aspect ratio analysis and imaging actin dynamics**

802   Laterally oriented embryos were used to measure the maximal length and width of

803   macrophages expressing *UAS-CLIP::GFP* under the control of *srpHemoGal4*. Briefly, 3D-

804   stacks with 1 μm Z resolution were acquired every 35-45 seconds for approximately 1 hour.

805   As the strength of the GAL4 expression increased over time, laser power was adjusted

806   during acquisition to reach the best possible quality of visualization. Images acquired from

807   mutiphoton microscopy were initially processed with ImSpector software (LaVision Bio

808   Tec) to compile channels from the imaging data.

809   We started measuring from the time the cell body of the first macrophage fully appeared at

810   the interface between the ectoderm and mesoderm and yolk sac until it had moved 30 μm

811   along the ectoderm mesoderm interface. At each timeframe, a line was drawn in Fiji along

812   the longest dimension of the macrophage in the direction of its front-rear polarization axis,

813   denoted the maximal cell length, and along the orthologonal longest dimension, which was

814   considered maximal cell width. We did not observe long CLIP::GFP protrusions, but when a

815   small protrusion was present, it was not included in the length measurement; within this gb

816   region the front of the first macrophage was clearly outlined with CLIP::GFP. The border

817   between the first and second entering macrophages was drawn based on the uninterrupted

818   intense line of CLIP::GFP at the base of the first macrophage; only cells with a clearly

819   visible border were measured. The length to width ratio was quantified for each timeframe

820   and a probability density function was plotted: 5 embryos were recorded for each genotype.

821

822   **Imaging the actin protrusion**

823   Laterally oriented embryos expressing *srpHemo-Gal4 UAS-LifeAct::GFP* were used to image

824   macrophage actin live with a 3D-stack resolution of 1μm. See above description of

825   CLIP::GFP labeled macrophage imaging for laser power and image compilation. Laser power

826   was also increased further in the DfosDN samples to enhance actin visualization. We

827   measured the length of the filopodia-like protrusion of the first entering macrophage with

828   Imaris software (Bitplane) from the time when the protrusion was inserted into the ectoderm,

829   mesoderm and yolk sac interface until the macrophage started to translocate its cell body into

830   that location.

Belyaeva et al

831

FACS sorting of macrophages

833 Adult flies of either *w;+;srpHemoGal4,srpHemo::3xmCherry/+* or *w;+;*

834 *srpHemoGal4,srpHemo::3xmCherry /UASDfosDN* genotypes were placed into plastic cages

835 closed with apple juice plates with applied yeast to enhance egg laying. Collections were

836 performed at 29°C for 1 hour, then kept at 29°C for additional 5 hours 15 minutes to reach

837 stage 11-early stage 12. Embryos were harvested for 2 days with 6-7 collections per day and

838 stored meanwhile at +4°C to slow down development. Collected embryos were dissociated

839 and the macrophages sorted as previously described (Gyoergy et al., 2018). About $1\text{-}1.5\text{x}10^5$

840 macrophages were sorted within 30 minutes.

841

Sequencing of the macrophage transcriptome

843 Total RNA was isolated from FACS-sorted macrophages using Qiagen RNeasy Mini kit (Cat

844 No. 74104). The quality and concentration of RNA was determined using Agilent 6000 Pico

845 kit (Cat No. 5067-1513) on an Agilent 2100 Bioanalyzer: on average about 100 ng of total

846 RNA was extracted from $1.5\text{x}10^5$ macrophages. RNA sequencing was performed by the CSF

847 facility of Vienna Biocenter according to standard procedures

848 (https://www.vbcf.ac.at/facilities/next-generation-sequencing/) on three replicates. Briefly,

849 the cDNA library was synthesized using QuantSeq 3' mRNA-seq Library Prep kit and

850 sequenced on the Illumina HiSeq 2500 platform. The reads were mapped to the *Drosophila*

851 *melanogaster* Ensembl BDGP6 reference genome with STAR (version 2.5.1b) The read

852 counts for each gene were detected using HTSeq (version 0.5.4p3). The Flybase annotation

853 (r6.19) was used in both mapping and read counting. Counts were normalised to arbitrary

854 units using the TMM normalization from edgeR package in R. Prior to statistical testing the

855 data was voom transformed and then the differential expression between the sample groups

33

Belyaeva et al

856   was calculated with limma package in R. The functional analyses were done using the topGO

857   and gage packages in R (Anders, Pyl, & Huber, 2015; Dobin et al., 2013).

Primer	Sequence
Fos_fw	ATGGTGAAGACCGTGTCAGG
Fos_rv	GTTGATCTGTCTCCGCTTGGA
Flna_fw	GTCACAGTGTCAATCGGAGGT
Flna_rv	TTGCCTGCTGCTTTTGTGTC
Flnb_fw	TTCTACACTGCTGCCAAGCC
Flnb_rv	CTGTAACCCAGGGCCTGAATC
Flnc_fw	CATCACCCGGAGTCCTTTCC
Flnc_rv	CTCTGTGCCCTTTGGACCTT
Tspan6_fw	TCGAACTAGTTGCCGCCATT
Tspan6_rv	CCGCAACAATGCAACGTACT
Gstt3_fw	GGAGCTCTACCTGGACCTGA
Gstt3_rv	AAGATGGCCACACTCTCTGC
Eva1c_fw	GTTGCCTACGCATGTGTTCC
Eva1c_rv	CCGATGCAGACACTGGACAT
Tspo_fw	GTATTCAGCCATGGGGTATGG
Tspo_rv	AAGCAGAAGATCGGCCAAGG
Tbp_fw	GGGGAGCTGTGATGTGAAGT
Tbp_rv	CCAGGAAATAATTCTGGCTCAT

858   **qRT-PCR analysis of mRNA levels in murine bones and osteosarcomas**

859   RNA isolation and qPCR was performed from bones of wild-type C57BL/6 mice and from

860   bones and osteosarcomas (OS) of H2-c-fosLTR as previously described with the above

861   primers (Rüther et al., 1989).

862

863   **Statistical and Repeatability**

864   Mouse experiments:

865   Data are shown as mean ± SEM. One-way ANOVA followed by Tukey's multiple

866   comparisons post-test was applied to compare experimental groups. Statistical analysis was

867   performed using GrapPad Prism 6.0 software. A p-value <0.05 was considered statistically

868   significant (*$p<0.05$, **$p<0.01$, ***$p<0.001$, ****$p<0.0001$).

869   *Drosophila* experiments:

870 Statistical tests as well as the number of embryos/cells/tracks/contacts assessed are listed in

871 the Figure legends. All statistical analyses were performed using GraphPad PRISM or R

872 Studio and significance was determined using a 95% confidence interval. No statistical

873 method was used to predetermine sample size. An unpaired t-test and Mann-Whitney U Test

874 were used to calculate the significance in differences between two groups and One-Way

875 ANOVA followed by Tukey HSD post hoc test was used for multiple comparisons.

876 Representative images of Dfos antibody staining were analyzed per replicate per genotype

877 and *in situ* hybridization are from experiments that were repeated 2 times with many

878 embryos with reproducible results. Representative images and plots of different *Dfos* mutants

879 in Fig 1 and S1 Fig are from experiments that were repeated 2-3 times. In live imaging

880 experiments in Fig 2 and S2 Fig, 3-7 embryos for each genotype were analyzed, each embryo

881 was recorded in a separate day. Three replicates were conducted of FACS sorting

882 macrophages from embryos, and then preparing RNA samples for RNA sequencing for each

883 genotype. Representative images and plots of RNAi and rescue experiments in Fig 4 and S4

884 Fig are from experiments that were repeated 2-3 times. Representative images and plots of

885 phalloidin immunostaining in Fig 4 are from experiments that were repeated 4 times. For all

886 immunostaining experiments 3-7 embryos were analyzed per replicate per genotype. In

887 Moe::3xmCherry experiments in Fig 4D, 11 and 12 embryos were analysed for the control

888 and *DfosDN*, and in Fig 4E 10, 8, and 8 embryos were analysed for the control, *cher RNAi*,

889 and *TM4SF RNAi* respectively, as indicated in the graph and in the relevant part of the F-

890 actin reporter measurement section of the methods. In the LifeAct::GFP protrusion live

891 imaging experiment in Fig 5 and S5 Fig, 3-5 embryos were analyzed for each genotype. In

892 CLIP::GFP live imaging experiments in Fig 5 and S5 Fig, 5-6 embryos were analyzed for

893 each genotype for the cell aspect ratio in germband zone, and 2 embryos in pre-germband

894 zone and for tracking of the front vs rear speed. Each embryo was recorded on a separate

895   day. The Lamin over expression in S5 Fig and the Lamin knockdown rescue experiments in

896   Fig 5G were repeated at least 3 times with reproducible results. Gb rescue experiment in Fig

897   5H was repeated at least 4 times with reproducible results.

898

Acknowledgements

References

918 Anders, S., Pyl, P. T., & Huber, W. (2015). HTSeq-A Python framework to work with high-throughput

919   sequencing data. *Bioinformatics*, *31*(2), 166–169. https://doi.org/10.1093/bioinformatics/btu638

920 Andrés, V., & González, J. M. (2009). Role of A-type lamins in signaling, transcription, and chromatin

921   organization. *Journal of Cell Biology*, *187*(7), 945–957. https://doi.org/10.1083/jcb.200904124

922 Bellanger, J. M., Astier, C., Sardet, C., Ohta, Y., Stossel, T. P., & Debant, A. (2000). The Rac1- and RhoG-

923   specific GEF domain of trio targets filamin to remodel cytoskeletal actin. *Nature Cell Biology*, *2*(12),

924   888–892. https://doi.org/10.1038/35046533

925 Benhra, N., Barrio, L., Muzzopappa, M., & Milán, M. (2018). Chromosomal Instability Induces Cellular

926   Invasion in Epithelial Tissues. *Developmental Cell*, *47*(2), 161-174.e4.

927   https://doi.org/10.1016/j.devcel.2018.08.021

928 Berditchevski, F., & Odintsova, E. (1999). Characterization of integrin-tetraspanin adhesion complexes: Role of

929   tetraspanins in integrin signaling. *Journal of Cell Biology*, *146*(2), 477–492.

930   https://doi.org/10.1083/jcb.146.2.477

931 Bershadsky, A. D., Balaban, N. Q., & Geiger, B. (2003). Adhesion-Dependent Cell Mechanosensitivity. *Annual*

932   *Review of Cell and Developmental Biology*, *19*(1), 677–695.

933   https://doi.org/10.1146/annurev.cellbio.19.111301.153011

934 Bilancia, C. G., Winkelman, J. D., Tsygankov, D., Nowotarski, S. H., Sees, J. A., Comber, K., … Peifer, M.

935   (2014). Enabled negatively regulates diaphanous-driven actin dynamics in vitro and in vivo.

936   *Developmental Cell*, *28*(4), 394–408. https://doi.org/10.1016/j.devcel.2014.01.015

937 Bosch, P.S., Makhijani, K., Herboso, L., Gold, K.S., Baginsky, R., Woodcock, K.J., Alexander, B., Kukar, K.,

938   Corcoran, S., Jacobs, T., Ouyang, D., Wong, C., Ramond, E.J.V., Rhiner, C., Moreno, E., Lemaitre, B.,

939   Geissmann, F., & Brueckner, K. (2019). Adult *Drosophila* lack hematopoiesis but rely on a blood cell

940   reservoir at the respiratory epithelia to relay infection signals to surrounding tissues. *Developmental Cell*,

941   *51*(6)787-803.

942   https://doi.org/10.1016/j.devcel.2019.10.017

943 Brock, A. R., Wang, Y., Berger, S., Renkawitz-Pohl, R., Han, V. C., Wu, Y., & Galko, M. J. (2012).

944   Transcriptional regulation of profilin during wound closure in Drosophila larvae. *Journal of Cell Science*,

945   *125*(23), 5667–5676. https://doi.org/10.1242/jcs.107490

946 Brückner, K., Kockel, L., Duchek, P., Luque, C. M., Rørth, P., & Perrimon, N. (2004). The PDGF/VEGF

947   receptor controls blood cell survival in Drosophila. *Developmental Cell*, *7*(1), 73–84.

948   https://doi.org/10.1016/j.devcel.2004.06.007

949   Brzozowski, J. S., Bond, D. R., Jankowski, H., Goldie, B. J., Burchell, R., Naudin, C., … Weidenhofer, J.

950   (2018). Extracellular vesicles with altered tetraspanin CD9 and CD151 levels confer increased prostate

951   cell motility and invasion. *Scientific Reports*, *8*(1). https://doi.org/10.1038/s41598-018-27180-z

952   Butcher, D.T., Alliston, T. & Weaver, V.M.(2009). A tense situation: forcing tumour progression. *Nature*

953   *Reviews Cancer, 9*(2), 108-22. . https://doi.org/10.11038/nrc2544

954   Cho, N. K., Keyes, L., Johnson, E., Heller, J., Ryner, L., Karim, F., & Krasnow, M. A. (2002). Developmental

955   control of blood cell migration by the Drosophila VEGF pathway. *Cell*, *108*(6).

956   https://doi.org/10.1016/S0092-8674(02)00676-1

957   Chugh, P., Clark, A. G., Smith, M. B., Cassani, D. A. D., Dierkes, K., Ragab, A., … Paluch, E. K. (2017). Actin

958   cortex architecture regulates cell surface tension. *Nature Cell Biology*, *19*(6), 689–697.

959   https://doi.org/10.1038/ncb3525

960   Danuser, G., Allard, J., & Mogilner, A. (2013). Mathematical Modeling of Eukaryotic Cell Migration: Insights

961   Beyond Experiments. *Annual Review of Cell and Developmental Biology*, *29*(1).

962   https://doi.org/10.1146/annurev-cellbio-101512-122308

963   Davidson, A. J., Millard, T. H., Evans, I. R., & Wood, W. (2019). Ena orchestrates remodelling within the actin

964   cytoskeleton to drive robust Drosophila macrophage chemotaxis. *Journal of Cell Science*, *132*(5).

965   https://doi.org/10.1242/jcs.224618

966   Davidson, P.M., Denais, C., Bakshi, M., & Lammerding, J. (2014).. Nuclear deformability constitutes a rate-

967   limiting step during cell migration in 3-D environments. *Cellular and Molecular Bioengineering,*

968   *7*(3)293-306. https://doi.org/10.1007/s12195-014-0342-y

969   Davis, J. R., Luchici, A., Miodownik, M., Stramer, B. M., Davis, J. R., Luchici, A., … Stramer, B. M. (2015).

970   Inter-Cellular Forces Orchestrate Contact Inhibition of Locomotion Article Inter-Cellular Forces

971   Orchestrate Contact Inhibition of Locomotion. *Cell*, *161*(2), 361–373.

972   https://doi.org/10.1016/j.cell.2015.02.015

973   Delaguillaumie, A., Lagaudrière-Gesbert, C., Popoff, M. R., & Conjeaud H., H. (2002). Rho GTPase link

974   cytoskeletal rearrangements and activation processes induced via the tetraspanin CD82 in T lymphocytes.

975   *Journal of Cell Science*, *115*(2).

976   Deluca, T. F., Cui, J., Jung, J. Y., St. Gabriel, K. C., & Wall, D. P. (2012). Roundup 2.0: Enabling comparative

977   genomics for over 1800 genomes. *Bioinformatics*, *28*(5). https://doi.org/10.1093/bioinformatics/bts006

978   Dobin, A., Davis, C. A., Schlesinger, F., Drenkow, J., Zaleski, C., Jha, S., … Gingeras, T. R. (2013). STAR:

979   Ultrafast universal RNA-seq aligner. *Bioinformatics*, *29*(1), 15–21.

980   https://doi.org/10.1093/bioinformatics/bts635

981   Duffy, J. B. (2002). GAL4 system in Drosophila: A fly geneticist's Swiss army knife. *Genesis*, *34*(1–2), 1–15.

982   https://doi.org/10.1002/gene.10150

983   Edwards, K. A., Demsky, M., Montague, R. A., Weymouth, N., & Kiehart, D. P. (1997). GFP-moesin

984   illuminates actin cytoskeleton dynamics in living tissue and demonstrates cell shape changes during

985   morphogenesis in Drosophila. *Developmental Biology*, *191*(1). https://doi.org/10.1006/dbio.1997.8707

986   Ehrlicher, A. J., Nakamura, F., Hartwig, J. H., Weitz, D. A., & Stossel, T. P. (2011). Mechanical strain in actin

987   networks regulates FilGAP and integrin binding to filamin A. *Nature*, *478*(7368), 260–263.

988   https://doi.org/10.1038/nature10430

989   Eresh, S., Riese, J., Jackson, D. B., Bohmann, D., & Bienz, M. (1997). A CREB-binding site as a target for

990   decapentaplegic signalling during Drosophila endoderm induction. *EMBO Journal*, *16*(8), 2014–2022.

991   https://doi.org/10.1093/emboj/16.8.2014

992   Evans, I. R., & Wood, W. (2011). Drosophila embryonic hemocytes. *Current Biology*, *21*(5), R173–R174.

993   https://doi.org/10.1016/j.cub.2011.01.061

994   Franck, Z., Gary, R., & Bretscher, A. (1993). Moesin, like ezrin, colocalizes with actin in the cortical

995   cytoskeleton in cultured cells, but its expression is more variable. *Journal of Cell Science*, *105*(1).

996   Fujita, M., Mitsuhashi, H., Isogai, S., Nakata, T., Kawakami, A., Nonaka, I., … Kudo, A. (2012). Filamin C

997   plays an essential role in the maintenance of the structural integrity of cardiac and skeletal muscles,

998   revealed by the medaka mutant zacro. *Developmental Biology*, *361*(1), 79–89.

999   https://doi.org/10.1016/j.ydbio.2011.10.008

1000 García-Echeverría, C. Methionine-containing zipper peptides. *Lett Pept Sci* **4,** 135–140 (1997).

1001   https://doi.org/10.1007/BF02443525

1002 Ginhoux, F.& Guilliams, M. (2016). Tissue-resident macrophage ontogeny and homeostasis. *Immunity 44*(3),

1003   439-449. https://doi.org/10.1016/j.immuni.2016.02.024

1004 Glogauer, M., Arora, P., Chou, D., Janmey, P. A., Downey, G. P., & McCulloch, C. A. G. (1998). The role of

1005   actin-binding protein 280 in integrin-dependent mechanoprotection. *Journal of Biological Chemistry*,

1006   *273*(3), 1689–1698. https://doi.org/10.1074/jbc.273.3.1689

1007   Glover, J.N.M. and Harrison, S.C. (1005). Crystal structure of the heterodimeric bZIP transcritpion factor c-Fos-

1008   c-Jun bound to DNA. *Nature, 373*(6511):257-261. https://doi.org/10.1038/373257a0

1009   Goldmann, W. H., Tempel, M., Sprenger, I., Isenberg, G., & Ezzell, R. M. (1997). Viscoelasticity of actin-

1010   gelsolin networks in the presence of filamin. *European Journal of Biochemistry*, *246*(2), 373–379.

1011   https://doi.org/10.1111/j.1432-1033.1997.00373.x

1012   Gonzalez-Gaitan, M. & Peifer, M. (2009) Exploring the roles of Diaphanous and Enabled activity in shaping the

1013   balance between filopodia and lamellipodia. *Molecular Biology of the Cell 20*(24).

1014   https://doi.org/10.1091/mbc.e09-02-0144

1015   Greten, F.R. & Grovennikov, S.I. (2019). Inflammation and Cancer: Triggers, Mechanisms and Consequences.

1016   *Immunity 51*(1), 27-41. https://doi.org/10.1016/j.immuni.2019.06.025

1017   Großhans, J., Wenzl, C., Herz, H. M., Bartoszewski, S., Schnorrer, F., Vogt, N., … Müller, H. A. (2005).

1018   RhoGEF2 and the formin Dia control the formation of the furrow canal by directed actin assembly during

1019   Drosophila cellularisation. *Development*, *132*(5), 1009–1020. https://doi.org/10.1242/dev.01669

1020   Guilliams, M., Thierry, G.R., Bonnardel, J., & Bajenoff, M. (2020). Establishment and Maintenance of the

1021   Macrophage Niche. *Immunity 52*(3), 434-451. https://doi.org/10.1016/j.immuni.2020.02.015

1022   Gyoergy, A., Roblek, M., Ratheesh, A., Valoskova, K., Belyaeva, V., Wachner, S., … Siekhaus, D. E. (2018).

1023   Tools allowing independent visualization and genetic manipulation of Drosophila melanogaster

1024   macrophages and surrounding tissues. *G3: Genes, Genomes, Genetics*, *8*(3).

1025   https://doi.org/10.1534/g3.117.300452

1026   Hammonds, A. A. S., Bristow, C. C. a, Fisher, W. W., Weiszmann, R., Wu, S., Hartenstein, V., … Celniker, S.

1027   E. (2013). Spatial expression of transcription factors in Drosophila embryonic organ development.

1028   *Genome Biology*, *14*(12), R140. https://doi.org/10.1186/gb-2013-14-12-r140

1029   Harada, T., Swift, J., Irianto, J., Shin, J, Spinler, K.R., Athirasala, A., Diegmiller, R., Dingal, P.C.D.P.,

1030   Ivanovska, I.L., & Discher, D.E. (2014). Nuclear lamin stiffness is a barrier to 3D migration, but softness

1031   can limit survival. J. Cell Biology, 2014(5)669-82. https://doi.org/10.1083/jcb.201308029.

1032   Heer, N. C., & Martin, A. C. (2017). Tension, contraction and tissue morphogenesis. *Development (Cambridge)*,

1033   *144*(23). https://doi.org/10.1242/dev.151282

1034   Holz, A., Bossinger, B., Strasser, T., Janning, W., & Klapper, R. (2003). The two origins of hemocytes in

1035   *Drosophila. Development, 130*(20), 4955-62. https://doi.org/10.1242/dev.007202

1036   Hong, I. K., Jeoung, D. Il, Ha, K. S., Kim, Y. M., & Lee, H. (2012). Tetraspanin CD151 stimulates adhesion-

Belyaeva et al

1037 dependent activation of Ras, Rac, and Cdc42 by facilitating molecular association between β1 integrins

1038 and small GTPases. *Journal of Biological Chemistry*, *287*(38), 32027–32039.

1039 https://doi.org/10.1074/jbc.M111.314443

1040 Hu, J., Lu, J., Lian, G., Ferland, R. J., Dettenhofer, M., & Sheen, V. L. (2014). Formin 1 and filamin B

1041 physically interact to coordinate chondrocyte proliferation and differentiation in the growth plate. *Human*

1042 *Molecular Genetics*, *23*(17), 4663–4673. https://doi.org/10.1093/hmg/ddu186

1043 Kasza, K. E., Broedersz, C. P., Koenderink, G. H., Lin, Y. C., Messner, W., Millman, E. A., … Weitz, D. A.

1044 (2010). Actin filament length tunes elasticity of flexibly cross-linked actin networks. *Biophysical Journal*,

1045 *99*(4), 1091–1100. https://doi.org/10.1016/j.bpj.2010.06.025

1046 Kessenbrock, K., Plaks, V., & Werb, Z. (2010). Matrix metalloproteinases: regulators of the tumor

1047 microenvironment. *Cell 141*(1), 52-67. https://doi.org/10.1016/j.cell.2010.03.015

1048 Kühn, S., & Geyer, M. (2014). Formins as effector proteins of rho GTPases. *Small GTPases*, *5*(JUNE).

1049 https://doi.org/10.4161/sgtp.29513

1050 Külshammer, E., Mundorf, J., Kilinc, M., Frommolt, P., Wagle, P., & Uhlirova, M. (2015). Interplay among

1051 Drosophila transcription factors Ets21c, Fos and Ftz-F1 drives JNK-mediated tumor malignancy. *DMM*

1052 *Disease Models and Mechanisms*, *8*(10), 1279–1293. https://doi.org/10.1242/dmm.020719

1053 Külshammer, E., & Uhlirova, M. (2013). The actin cross-linker Filamin/Cheerio mediates tumor malignancy

1054 downstream of JNK signaling. *Journal of Cell Science*, *126*(4), 927–938.

1055 https://doi.org/10.1242/jcs.114462

1056 Kumar, A., Shutova, M. S., Tanaka, K., Iwamoto, D. V., Calderwood, D. A., Svitkina, T. M., & Schwartz, M.

1057 A. (2019). Filamin A mediates isotropic distribution of applied force across the actin network. *Journal of*

1058 *Cell Biology*, *218*(8), 2481–2491. https://doi.org/10.1083/jcb.201901086

1059 Lehmann, R., & Tautz, D. (1994). In Situ Hybridization to RNA. *Methods in Cell Biology*, *44*(C), 575–596.

1060 https://doi.org/10.1016/S0091-679X(08)60933-4

1061 Lemaitre, B., & Hoffmann, J. (2007). The Host Defense of *Drosophila melanogaster*. *Annual Review of*

1062 *Immunology*, *25*(1), 697–743. https://doi.org/10.1146/annurev.immunol.25.022106.141615

1063 Lesch, C., Jo, J., Wu, Y., Fish, G. S., & Galko, M. J. (2010). A Targeted *UAS-RNAi* Screen in Drosophila

1064 Larvae Identifies Wound Closure Genes Regulating Distinct Cellular Processes. *Genetics*, *186*(3), 943–

1065 957. https://doi.org/10.1534/genetics.110.121822

1066 Lian, G., Dettenhofer, M., Lu, J., Downing, M., Chenn, A., Wong, T., & Sheen, V. (2016). Filamin A- and

1067   formin 2-dependent endocytosis regulates proliferation via the canonical wnt pathway. *Development*

1068   *(Cambridge)*, *143*(23). https://doi.org/10.1242/dev.139295

1069   Linder, M., Glitzner, E., Srivatsa, S., Bakiri, L., Matsuoka, K., Shahrouzi, P., … Sibilia, M. (2018). EGFR is

1070   required for FOS☐dependent bone tumor development via RSK2/CREB signaling. *EMBO Molecular*

1071   *Medicine*, *10*(11). https://doi.org/10.15252/emmm.201809408

1072   Luster, A. D., Alon, R., & von Andrian, U. H. (2005). Immune cell migration in inflammation: Present and

1073   future therapeutic targets. *Nature Immunology*, *6*(12), 1182–1190. https://doi.org/10.1038/ni1275

1074   Makhijani, K., Alexander, B., Tanaka, T., Rulfson, E., & Brückner, K. (2011). The peripheral nervous system

1075   supports blood cell homing and survival in the Drosophila larva. *Development, 138*(24), 5379-91.

1076   https://doi.org/10.1242/dev.067322

1077   Matsubayashi, Y., Louani, A., Dragu, A., Sánchez-Sánchez, B. J., Serna-Morales, E., Yolland, L., … Stramer,

1078   B. M. (2017). A Moving Source of Matrix Components Is Essential for De Novo Basement Membrane

1079   Formation. *Current Biology*, *27*(22), 3526-3534.e4. https://doi.org/10.1016/j.cub.2017.10.001

1080   Min, P. I., Spurney, R. F., Qisheng, T. U., Hinson, T., & Darryl Quarles, L. (2002). Calcium-sensing receptor

1081   activation of Rho involves filamin and rho-guanine nucleotide exchange factor. *Endocrinology*, *143*(10),

1082   3830–3838. https://doi.org/10.1210/en.2002-220240

1083   Mitchison, T.J., and Cramer, L.P. (1996) Actin-based cell motility and cell locomotion. *Cell 84*(3)371-9).

1084   https://doi.org/10.1016/s0092-8864(00)81281-7.

1085   Muñoz-Alarcón, A., Pavlovic, M., Wismar, J., Schmitt, B., Eriksson, M., Kylsten, P., & Dushay, M. S. (2007).

1086   Characterization of lamin mutation phenotypes in Drosophila and comparison to human laminopathies.

1087   *PloS One*, *2*(6). https://doi.org/10.1371/journal.pone.0000532

1088   Ohta, Y., Suzuki, N., Nakamura, S., Hartwig, J. H., & Stossel, T. P. (1999). The small GTPase RaIA targets

1089   filamin to induce filopodia. *Proceedings of the National Academy of Sciences of the United States of*

1090   *America*, *96*(5), 2122–2128. https://doi.org/10.1073/pnas.96.5.2122

1091   Paluch, E. K., Aspalter, I. M., & Sixt, M. (2016). Focal Adhesion–Independent Cell Migration. *Annual Review*

1092   *of Cell and Developmental Biology*, *32*(1), 469–490. https://doi.org/10.1146/annurev-cellbio-111315-

1093   125341

1094   Perez-Hernandez, D., Gutiérrez-Vázquez, C., Jorge, I., López-Martín, S., Ursa, A., Sánchez-Madrid, F., …

1095   Yañez-Mó, M. (2013). The intracellular interactome of tetraspanin-enriched microdomains reveals their

1096   function as sorting machineries toward exosomes. *Journal of Biological Chemistry*, *288*(17), 11649–

1097   11661. https://doi.org/10.1074/jbc.M112.445304

1098 Perkins, L. A., Holderbaum, L., Tao, R., Hu, Y., Sopko, R., McCall, K., … Perrimon, N. (2015). The transgenic

1099   RNAi project at Harvard medical school: Resources and validation. *Genetics*, *201*(3), 843–852.

1100   https://doi.org/10.1534/genetics.115.180208

1101 Popowicz, G. M., Schleicher, M., Noegel, A. A., & Holak, T. A. (2006). Filamins: promiscuous organizers of

1102   the cytoskeleton. *Trends in Biochemical Sciences*, *31*(7), 411–419.

1103   https://doi.org/10.1016/j.tibs.2006.05.006

1104 Raab, M., Gentili, M., de Belly, H., Thiam, H.R., Vargas, P., Jimenez, A.J., Lautenschlaeger, F., Voituriez, R.,

1105   Lennon-Duménil, A.M., Manel, N, Piel, M. (2016). ESCRT III repairs nuclear envelope ruptures during

1106   cell migration to limit DNA damage and cell death. Science, 352(6283), 359-62.

1107   https://doi.org/10.1126/science.aad7611

1108 Ratheesh, A., Belyaeva, V., & Siekhaus, D. E. (2015). Drosophila immune cell migration and adhesion during

1109   embryonic development and larval immune responses. *Current Opinion in Cell Biology*, *36*, 71–79.

1110   https://doi.org/10.1016/j.ceb.2015.07.003

1111 Ratheesh, A., Biebl, J., Vesela, J., Smutny, M., Papusheva, E., Krens, S. F. G., … Siekhaus, D. E. (2018).

1112   Drosophila TNF Modulates Tissue Tension in the Embryo to Facilitate Macrophage Invasive Migration.

1113   *Developmental Cell*, *45*(3), 331-346.e7. https://doi.org/10.1016/j.devcel.2018.04.002

1114 Razinia, Z., Mäkelä, T., Ylänne, J., & Calderwood, D. A. (2012). Filamins in Mechanosensing and Signaling.

1115   *Annual Review of Biophysics*, *41*(1), 227–246. https://doi.org/10.1146/annurev-biophys-050511-102252

1116 Riesgo-Escovar, J. R., & Hafen, E. (1997). Common and distinct roles of DFos and DJun during Drosophila

1117   development. *Science (New York, N.Y.)*, *278*(5338), 669–672.

1118   https://doi.org/10.1126/science.278.5338.669

1119 Riveline, D., Zamir, E., Balaban, N. Q., Schwarz, U. S., Ishizaki, T., Narumiya, S., … Bershadsky, A. D.

1120   (2001). Focal contacts as mechanosensors: Externally applied local mechanical force induces growth of

1121   focal contacts by an mDia1-dependent and ROCK-independent mechanism. *Journal of Cell Biology*,

1122   *153*(6), 1175–1185. https://doi.org/10.1083/jcb.153.6.1175

1123 Rose, R., Weyand, M., Lammers, M., Ishizaki, T., Ahmadian, M. R., & Wittinghofer, A. (2005). Structural and

1124   mechanistic insights into the interaction between Rho and mammalian Dia. *Nature*, *435*(7041), 513–518.

1125   https://doi.org/10.1038/nature03604

1126 Rousso, T., Shewan, A. M., Mostov, K. E., Schejter, E. D., & Shilo, B. Z. (2013). Apical targeting of the formin

1127   diaphanous in Drosophila tubular epithelia. *ELife*, *2013*(2). https://doi.org/10.7554/eLife.00666

1128   Sánchez-Sánchez, B. J., Urbano, J. M., Comber, K., Dragu, A., Wood, W., Stramer, B., & Martín-Bermudo, M.

1129   D. (2017). Drosophila Embryonic Hemocytes Produce Laminins to Strengthen Migratory Response. *Cell*

1130   *Reports*, *21*(6), 1461–1470. https://doi.org/10.1016/j.celrep.2017.10.047

1131   Seth, A., Otomo, C., & Rosen, M. K. (2006). Autoinhibition regulates cellular localization and actin assembly

1132   activity of the diaphanous-related formins FRLα and mDia1. *Journal of Cell Biology*, *174*(5), 701–713.

1133   https://doi.org/10.1083/jcb.200605006

1134   Sharma, P. & Allison, J.P. (2015) The future of immune checkpoint therapy. *Science 348*(6230), 56-61.

1135   https://doi.org/10.1126/science.aaa8172.

1136   Shigeta, M., Sanzen, N., Ozawa, M., Gu, J., Hasegawa, H., & Sekiguchi, K. (2003). CD151 regulates epithelial

1137   cell-cell adhesion through PKC- and Cdc42-dependent actin cytoskeletal reorganization. *Journal of Cell*

1138   *Biology*, *163*(1), 165–176. https://doi.org/10.1083/jcb.200301075

1139   Siekhaus, D., Haesemeyer, M., Moffitt, O., & Lehmann, R. (2010). RhoL controls invasion and Rap1

1140   localization during immune cell transmigration in Drosophila. *Nature Cell Biology*, *12*(6), 605–610.

1141   https://doi.org/10.1038/ncb2063

1142   Sit, S. T., & Manser, E. (2011). Rho GTPases and their role in organizing the actin cytoskeleton. *Journal of Cell*

1143   *Science*, *124*(5), 679–683. https://doi.org/10.1242/jcs.064964

1144   Smutny, M., Ákos, Z., Grigolon, S., Shamipour, S., Ruprecht, V., Čapek, D., … Heisenberg, C. P. (2017).

1145   Friction forces position the neural anlage. *Nature Cell Biology*, *19*(4), 306–317.

1146   https://doi.org/10.1038/ncb3492

1147   Sokol, N. S., & Cooley, L. (2003). Drosophila filamin is required for follicle cell motility during oogenesis.

1148   *Developmental Biology*, *260*(1), 260–272. https://doi.org/10.1016/S0012-1606(03)00248-3

1149   Somogyi, K., & Rørth, P. (2004). Evidence for tension-based regulation of Drosophila MAL and SRF during

1150   invasive cell migration. *Developmental Cell*, *7*(1), 85–93. https://doi.org/10.1016/j.devcel.2004.05.020

1151   Stossel, T. P., Condeelis, J., Cooley, L., Hartwig, J. H., Noegel, A., Schleicher, M., & Shapiro, S. S. (2001).

1152   Filamins as integrators of cell mechanics and signalling. *Nature Reviews Molecular Cell Biology*, *2*(2),

1153   138–145. https://doi.org/10.1038/35052082

1154   Szabo, P.A., Miron, M., & Farber, D.L. (2019). Location, location, location: Tissue residence memory T cells in

1155   mice and humans. *Science Immunology 4*(34), https://doi.org/10.1126/scieimunol.aas9673

1156   Szalóki, N., Krieger, J. W., Komáromi, I., Tóth, K., & Vámosi, G. (2015). Evidence for Homodimerization of
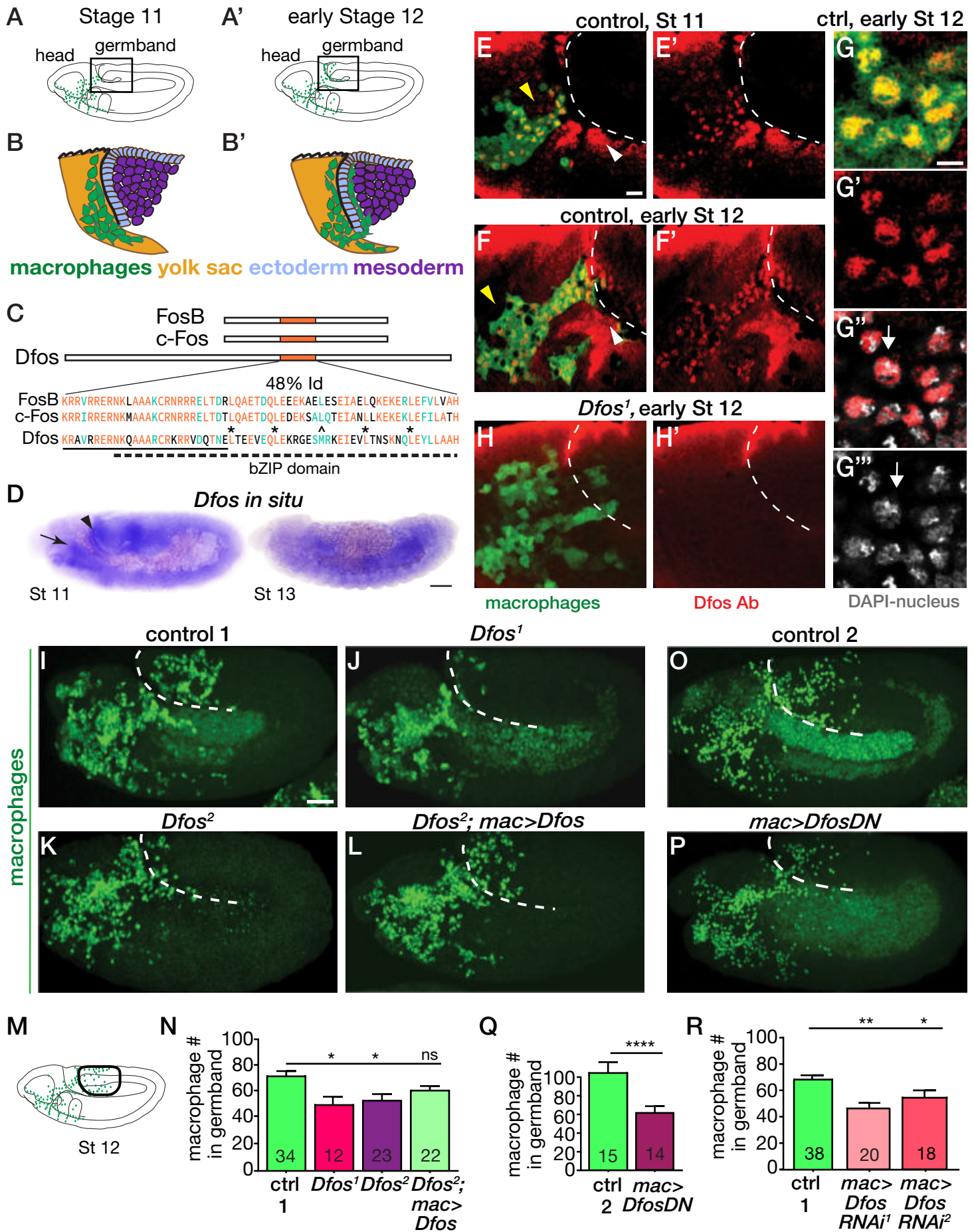
Belyaeva et al

1157   the c-Fos Transcription Factor in Live Cells Revealed by Fluorescence Microscopy and Computer

1158   Modeling. *Molecular and Cellular Biology*, *35*(21). https://doi.org/10.1128/mcb.00346-15

1159   Tejera, E., Rocha-Perugini, V., López-Martín, S., Ṕrez-Hernández, D., Bachir, A. I., Horwitz, A. R., … Yáñez-

1160   Mo, M. (2013). CD81 regulates cell migration through its association with Rac GTPase. *Molecular*

1161   *Biology of the Cell*, *24*(3), 261–273. https://doi.org/10.1091/mbc.E12-09-0642

1162   Termini, C. M., & Gillette, J. M. (2017). Tetraspanins Function as Regulators of Cellular Signaling. *Frontiers in*

1163   *Cell and Developmental Biology*, *5*, 34. https://doi.org/10.3389/fcell.2017.00034

1164   Theret, M., Mounier, R., & Rossi, F. (2019). The origins and non-canonical functions of macrophages in

1165   development and regeneration. *Development, 146*(9). https://doi.org/10.1242/dev.156000

1166   Thiam, H., Vargas, P., Carpi, N., Crespo, C.L., Raab, M., Terriac, E., King, M.C., Jacobelli, J., Alberts, A.S.,

1167   Stradal, T., Lennon-Dumenil, A., Piel, M. (2016). Perinuclear Arp2/3-driven actin polymerization enables

1168   nuclear deformation to facilitate cell migration through complex environments. Stremmel:10997,

1169   https://doi.org/10.1038/ncomms10997

1170   Thurmond, J., Goodman, J. L., Strelets, V. B., Attrill, H., Gramates, L. S., Marygold, S. J., … Baker, P. (2019).

1171   FlyBase 2.0: The next generation. *Nucleic Acids Research*, *47*(D1). https://doi.org/10.1093/nar/gky1003

1172   Tomancak, P., Beaton, A., Weiszmann, R., Kwan, E., Shu, S. Q., Lewis, S. E., … Rubin, G. M. (2002).

1173   Systematic determination of patterns of gene expression during Drosophila embryogenesis. *Genome*

1174   *Biology*, *3*(12). https://doi.org/10.1186/gb-2002-3-12-research0088

1175   Tomancak, P., Berman, B. P., Beaton, A., Weiszmann, R., Kwan, E., Hartenstein, V., … Rubin, G. M. (2007).

1176   Global analysis of patterns of gene expression during Drosophila embryogenesis. *Genome Biology*, *8*(7).

1177   https://doi.org/10.1186/gb-2007-8-7-r145

1178   Tseng, Y., An, K. M., Esue, O., & Wirtz, D. (2004). The Bimodal Role of Filamin in Controlling the

1179   Architecture and Mechanics of F-actin Networks. *Journal of Biological Chemistry*, *279*(3), 1819–1826.

1180   https://doi.org/10.1074/jbc.M306090200

1181   Uhlirova, M., & Bohmann, D. (2006). JNK- and Fos-regulated Mmp1 expression cooperates with Ras to induce

1182   invasive tumors in Drosophila. *EMBO Journal*, *25*(22), 5294–5304.

1183   https://doi.org/10.1038/sj.emboj.7601401

1184   Vadlamudi, R. K., Li, F., Adam, L., Nguyen, D., Ohta, Y., Stossel, T. P., & Kumar, R. (2002). Filamin is

1185   essential in actin cytoskeletal assembly mediated by p21-activated kinase 1. *Nature Cell Biology*, *4*(9),
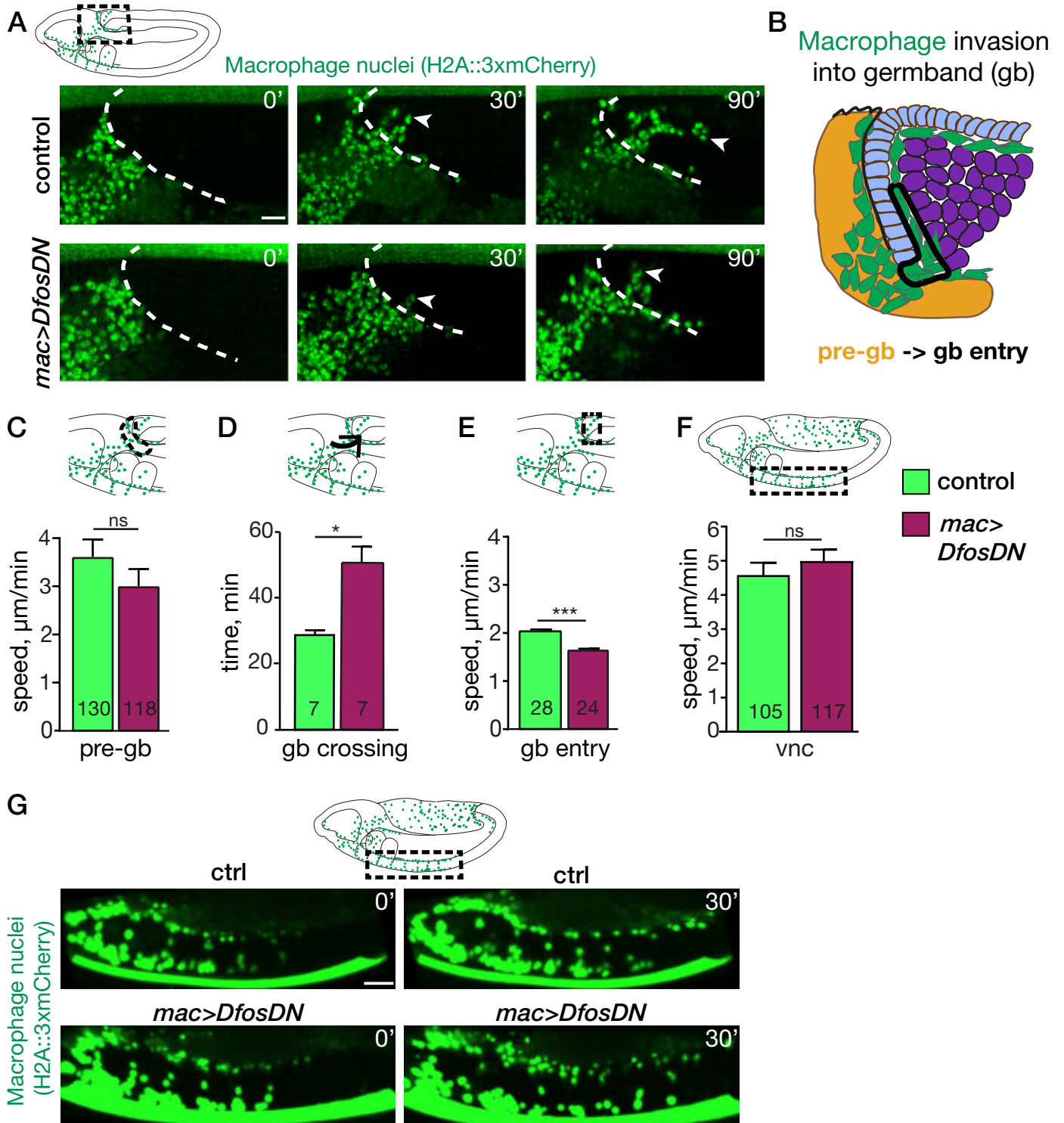
1186   681–690. https://doi.org/10.1038/ncb838

1187   Valoskova, K., Biebl, J., Roblek, M., Emtenani, S., Gyoergy, A., Misova, M., … Siekhaus, D. E. (2019). A

1188   conserved major facilitator superfamily member orchestrates a subset of O-glycosylation to aid

1189   macrophage tissue invasion. *ELife*, *8*. https://doi.org/10.7554/eLife.41801

1190   Vetter, I.R., & Wittinghofer, A. (2001). The guanine nucleotide-binding switch in three dimensions. *Science*

1191   *294(*5545),1299-1304. https://doi.org/10.1126/science.1062023

1192   Warner, S. J., & Longmore, G. D. (2009). Cdc42 antagonizes Rho1 activity at adherens junctions to limit

1193   epithelial cell apical tension. *Journal of Cell Biology*, *187*(1), 119–133.

1194   https://doi.org/10.1083/jcb.200906047

1195   Weavers, H., Evans, I. R., Martin, P., & Wood, W. (2016). Corpse Engulfment Generates a Molecular Memory

1196   that Primes the Macrophage Inflammatory Response. *Cell*. https://doi.org/10.1016/j.cell.2016.04.049

1197   Williams, M. J., Habayeb, M. S., & Hultmark, D. (2007). Reciprocal regulation of Rac1 and Rho1 in Drosophila

1198   circulating immune surveillance cells. *Journal of Cell Science*, *120*(3), 502–511.

1199   https://doi.org/10.1242/jcs.03341

1200   Wintner, O., Hirsch-Attas, N., Schlossberg, M., Brofman, F., Friedman, R., Kupervaser, M., … Buxboim, A.

1201   (2020). A Unified Linear Viscoelastic Model of the Cell Nucleus Defines the Mechanical Contributions of

1202   Lamins and Chromatin. *Advanced Science*, *7*(8). https://doi.org/10.1002/advs.201901222

1203   Wood, W., Faria, C., & Jacinto, A. (2006). Distinct mechanisms regulate hemocyte chemotaxis during

1204   development and wound healing in Drosophila melanogaster. *Journal of Cell Biology*, *173*(3).

1205   https://doi.org/10.1083/jcb.200508161

1206   Yáñez-Mó, M., Barreiro, O., Gordon-Alonso, M., Sala-Valdés, M., & Sánchez-Madrid, F. (2009). Tetraspanin-

1207   enriched microdomains: a functional unit in cell plasma membranes. *Trends in Cell Biology*, *19*(9), 434–

1208   446. https://doi.org/10.1016/j.tcb.2009.06.004

1209   Yeung, L., Hickey, M.J., & Wright, M.D. (2018) The many and varied roles of tetraspanins in immune cell

1210   recrutment and migration. Frontiers in Immunology.9:1644 .https:// doi: 10.3389/fimmu.2018.01644.

1211   Zeitlinger, J., Kockel, L., Peverali, F. A., Jackson, D. B., Mlodzik, M., & Bohmann, D. (1997). Defective dorsal

1212   closure and loss of epidermal decapentaplegic expression in Drosophila fos mutants. *EMBO Journal*,

1213   *16*(24), 7393–7401. https://doi.org/10.1093/emboj/16.24.7393

1214   Zhang, X. A., Bontrager, A. L., & Hemler, M. E. (2001). Transmembrane-4 Superfamily Proteins Associate

1215   with Activated Protein Kinase C (PKC) and Link PKC to Specific β1 Integrins. *Journal of Biological*

1216   *Chemistry*, *276*(27), 25005–25013. https://doi.org/10.1074/jbc.M102156200

1217   Zhou, J., Kim, H. Y., & Davidson, L. A. (2009). Actomyosin stiffens the vertebrate embryo during crucial

1218   stages of elongation and neural tube closure. *Development*, *136*(4), 677–688.

1219   https://doi.org/10.1242/dev.026211

1220   Zimmerman, B., Kelly, B., McMillan, B. J., Seegar, T. C. M., Dror, R. O., Kruse, A. C., & Blacklow, S. C.

1221   (2016). Crystal Structure of a Full-Length Human Tetraspanin Reveals a Cholesterol-Binding Pocket.

1222   *Cell*, *167*(4). https://doi.org/10.1016/j.cell.2016.09.056

1223   Zimmerman, B., Kelly, B., McMillan, B., Seegar, T., Kruse, A., & Blacklow, S. (2016). Crystal Structure of

1224   Human Tetraspanin CD81 Reveals a Conserved Intramembrane Binding Cavity. *Cell*, *167*(4), 1041–1051.

1225   https://doi.org/10.1016/j.cell.2016.09.056

1226   Zwerger, M., Jaalouk, D. E., Lombardi, M. L., Isermann, P., Mauermann, M., Dialynas, G., … Lammerding, J.

1227   (2013). Myopathic lamin mutations impair nuclear stability in cells and tissue and disrupt nucleo-

1228   cytoskeletal coupling. *Human Molecular Genetics*, *22*(12), 2335–2349. https://doi.org/10.109

1229

Belyaeva et al. Figure 1

A Stage 11 — head, germband

A' early Stage 12 — head, germband

B / **B'** macrophages · yolk sac · ectoderm · mesoderm

C FosB, c-Fos, Dfos — 48% Id

FosB KRRVRRERNKLAAAKCRNRRRELTDRLQAETDQLEEEKAELESEIAELQKEKERLEFVLVAH
c-Fos KRRIRRERNKMAAAKCRNRRRELTDTLQAETDQLEDEKSALQTEIANLLKEKEKLEFILATH
Dfos KRAVRRERNKQAAARCRKRRVDQTNELTEEVEQLEKRGESMRKEIEVLTNSKNQLEYLLAAH
bZIP domain

D *Dfos in situ* — St 11, St 13

E control, St 11 / **E'**

F control, early St 12 / **F'**

H *Dfos[1]*, early St 12 / **H'**

G ctrl, early St 12 / **G'** / **G''** / **G'''**

macrophages — Dfos Ab — DAPI-nucleus

control 1 **I** / *Dfos[1]* **J** / control 2 **O**

Dfos[2] **K** / *Dfos[2]; mac>Dfos* **L** / *mac>DfosDN* **P**

macrophages

M St 12

N macrophage # in germband — ctrl 1 (34), *Dfos[1]* (12), *Dfos[2]* (23), *Dfos[2]; mac>Dfos* (22) — * * ns

Q macrophage # in germband — ctrl 2 (15), *mac>DfosDN* (14) — ****

R macrophage # in germband — ctrl 1 (38), *mac>DfosRNAi[1]* (20), *mac>DfosRNAi[2]* (18) — ** *

A Macrophage nuclei (H2A::3xmCherry)

control — 0' — 30' — 90'

mac>DfosDN — 0' — 30' — 90'

B Macrophage invasion into germband (gb)

pre-gb -> gb entry

C pre-gb — speed, µm/min — ns — 130 — 118

D gb crossing — time, min — * — 7 — 7

E gb entry — speed, µm/min — *** — 28 — 24

F vnc — speed, µm/min — ns — 105 — 117

control

mac>DfosDN

G Macrophage nuclei (H2A::3xmCherry)

ctrl — 0' — ctrl — 30'

mac>DfosDN — 0' — mac>DfosDN — 30'

Belyaeva et al., Figure 3

A Early stage 12

control   mac>DfosDN

↓   ↓

FACS
macrophages

↓   ↓

RNA-Seq
gene expression

B

Gene	Possible Cellular Function	Mouse Ortholog Protein	Identity
cher	actin crosslinking	Filamin A	53%
CG42402	homophilic adhesion	Protein eva-1 homolog	35%
TM4SF	cell membrane organisation	Tetraspanin-6	24%
Xrp1	adhesion down-regulation	Epiglycan	22%
Dhc36C	cargo transport	Dynein axonemal, heavy chain 7C	57%
CG42260	ion transport	Cyclic nucleotide-gated olfact. channel	50%
Tspo	mitochondrial transport	Translocator protein	46%
GstT4	detoxification (glutathione transfer)	Glutathione S-transferase theta-3	39%
CG14204	acetyl-CoA metabolism	O-acetyltransferase like protein	27%
CG31337	proteolysis	no ortholog	NA

C *ctrl*

D *mac>TM4SF RNAi*

E *mac>cher RNAi*

F *mac>TM4SF RNAi,cher RNAi*

G

H *ctrl*

I *mac>DfosDN*

J *mac>DfosDN,cher*

K *mac>DfosDN,TM4SF*

L

M *Fos*

N *FlnA*

N' *FlnB*

N" *FlnC*

O *Tspan6*

Belyaeva et al, Figure 4

Belyaeva et al. Figure 6